



Importance of Non-uniform Boundary Migration for Recrystallization Kinetics

Lin, Fengxiang; Zhang, Yubin; Pantleon, Wolfgang; Juul Jensen, Dorte

Published in:

Metallurgical and Materials Transactions A: Physical Metallurgy and Materials Science

Link to article, DOI:

[10.1007/s11661-018-4846-2](https://doi.org/10.1007/s11661-018-4846-2)

Publication date:

2018

Document Version

Peer reviewed version

[Link back to DTU Orbit](#)

Citation (APA):

Lin, F., Zhang, Y., Pantleon, W., & Juul Jensen, D. (2018). Importance of Non-uniform Boundary Migration for Recrystallization Kinetics. *Metallurgical and Materials Transactions A: Physical Metallurgy and Materials Science*, 49(11), 5246-5258. <https://doi.org/10.1007/s11661-018-4846-2>

General rights

Copyright and moral rights for the publications made accessible in the public portal are retained by the authors and/or other copyright owners and it is a condition of accessing publications that users recognise and abide by the legal requirements associated with these rights.

- Users may download and print one copy of any publication from the public portal for the purpose of private study or research.
- You may not further distribute the material or use it for any profit-making activity or commercial gain
- You may freely distribute the URL identifying the publication in the public portal

If you believe that this document breaches copyright please contact us providing details, and we will remove access to the work immediately and investigate your claim.

Importance of non-uniform boundary migration for recrystallization kinetics

Fengxiang Lin^{*1}, Yubin Zhang², Wolfgang Pantleon², and Dorte Juul Jensen²

¹Université catholique de Louvain, Institute of Mechanics, Materials and Civil
Engineering (iMMC), 1348 Louvain la Neuve, Belgium

²Department of Mechanical Engineering, Technical University of Denmark, 2800 Kgs.
Lyngby, Denmark

Abstract

Recrystallization kinetics are studied by three characterization methods: post-mortem electron microscopy, in-situ three dimensional X-ray diffraction (3DXRD) and ex-situ electron microscopy. Cold-rolled copper is used as a model material. The post-mortem analysis shows that the average migration velocity of unimpinged recrystallizing boundaries decreases strongly with annealing time, leading to a low Avrami exponent. For individual grains, the in-situ 3DXRD measurement reveals that the growth rates decrease significantly shortly after nucleation. This is explained by the ex-situ characterizations, which show that different segments of the recrystallizing boundaries migrate with significantly different velocities, and some boundaries, although unimpinged, remain stationary. This non-uniform migration of recrystallizing boundaries leads to an amoeba-like growth, and is proposed to be responsible for the decrease of the average boundary migration velocity, because the fraction of slowly moving/stationary boundaries increases during the recrystallization. Reasons for stationary boundaries are discussed based on a quantitative analysis of the local deformed microstructure. It is concluded that non-uniform boundary migration has a significant influence on recrystallization kinetics and needs to be included in recrystallization models.

Keywords: Recrystallization, EBSD, 3DXRD, heterogeneity, grain boundary migration

*fengxiang.lin@uclouvain.be

1 Introduction

Recrystallization is of key importance for thermomechanical processing of metals and alloys. When a deformed metal is heat-treated, new nearly defect-free grains, here termed recrystallized grains, emerge and grow to replace the deformed matrix. After recrystallization, the density of dislocations introduced during deformation is largely reduced. Recrystallization typically also leads to a significant change in grain size, shape and texture compared to the deformed and the original material. It is thus one of the most effective approaches to alter the mechanical and physical properties of metals and alloys.

To control the recrystallization process, the transformation kinetics during recrystallization needs to be quantified. The classical model describing transformation kinetics was proposed by Johnson and Mehl [1], Avrami [2] and Kolmogorov [3] for phase transformations, but is generally used also for recrystallization. In this so-called JMAK model, the increase of the recrystallized volume fraction (V_V) during isothermal annealing is expressed as:

$$V_V = 1 - \exp(-kt^n) \quad (1)$$

where t is the annealing time, and k and n are two parameters. n is often termed the Avrami exponent. The theoretical derivation of the JMAK model assumes that the nucleation sites are randomly distributed in space. When all the recrystallized grains grow in 3D at a constant boundary migration velocity, the Avrami exponent n equals 3 for site saturated nucleation (i.e. all the nuclei appear instantaneously at the beginning of recrystallization), and n equals 4 for the situation of a constant nucleation rate. This is in the following referred to as the idealized JMAK model. Unfortunately, the idealized JMAK model often fails in two aspects: the exponent n has frequently been observed to have values much lower than 3 for 3D growth (e.g. [4]), and is not always constant throughout the recrystallization process, but varies as a function of time (e.g. [5]).

The shortcomings of the idealized JMAK model to describe typical recrystallization kinetics can be attributed to its assumptions. In reality, nucleation sites are often not randomly distributed. Local regions with high stored energy and large misorientations are preferred nucleation sites, e.g. regions near triple junctions [6, 7], transition bands [8], shear bands [9], and large secondary particles [10, 11]. Clustered nucleation, which in turn leads to early impingement of recrystallized grains, on average retards the recrystallization process, as compared to random nucleation. Moreover, migration velocities of the recrystallizing boundaries are often not constant but decrease with annealing time. For example, English and Backofen [12] reported an average boundary migration velocity decreasing as t^{-1} in hot-worked silicon iron. Others reported boundary migration velocities decreasing as $t^{-\alpha}$, with an exponent

54 α between 0 and 1 (e.g. [13, 14]).

55 Statistically, the nucleation and growth conditions during recrystallization can be deduced using
56 the Microstructural Path Method (MPM) suggested by Vandermeer et al. ([15]). This method relies
57 on a number of microstructural parameters determined experimentally for a series of partially recryst-
58 tallized samples using stereological principles. This type of post-mortem analysis gives an adequate
59 quantification of the *average* nucleation and growth conditions, but does not provide information on
60 the local physical mechanisms. Recently, in-situ and ex-situ experiments using advanced synchrotron
61 X-ray methods have been conducted mapping directly the nucleation and growth of individual grains.
62 For example, using 3D X-ray diffraction (3DXRD) [16–18] the nucleation incubation time and growth
63 rate of individual nuclei/grains can be determined for bulk samples. With near-field high-energy X-
64 ray diffraction microscopy (nf-HEDM)[19] and differential aperture X-ray microscopy (DAXM) [20], the
65 nucleation sites in the deformed matrix can be pinpointed. However, all these techniques are not suit-
66 able for characterization of hundreds of grains, which are necessary for a statistically-sound analysis of
67 recrystallization kinetics. Furthermore, in-situ and ex-situ experiments using electron microscopy ([21–
68 24]) have been performed. However, characterization on a 2D surface may not be representative for
69 bulk behaviour.

70 In this work, we propose a novel approach by combining three methods, namely post-mortem elec-
71 tron microscopy, in-situ 3DXRD and ex-situ electron microscopy, for a comprehensive analysis of re-
72 crystallization kinetics. This combined approach overcomes the major shortcomings of the individual
73 methods, and more importantly covers characterization on three different length scales: i) based on the
74 post-mortem characterization of a series of partially recrystallized samples, the nucleation and growth
75 conditions on the *sample* scale are identified through application of MPM; ii) in-situ 3DXRD monitors
76 the nucleation and growth for individual grains on the *grain* scale, and supports the MPM analysis; iii)
77 ex-situ electron microscopy investigates the *local* boundary migration during annealing and supports
78 the in-situ 3DXRD results. With this combined approach, we gain new insights in important details of
79 the recrystallization kinetics.

80 2 Experimental

81 2.1 Material

82 Oxygen free high conductivity copper was used in this study. We have chosen this material because it
83 has been extensively studied in the past but yet its recrystallization kinetics have not been successfully

84 explained, and it can serve as a model material for many typical metals. The chemical composition was
 85 measured using optical emission spectroscopy, and is listed in Table I. The starting material had a grain
 86 size of 22 μm , and a weak initial texture [18]. The sample was cold rolled to 90% reduction in thickness
 87 in several passes using a rolling mill with a roller diameter of 340 mm. The ratio of the contact length
 88 over the average thickness l/h was between 0.5 to 5 for each pass to ensure homogeneous rolling [25].
 89 The width of the rolling plate was wide enough to avoid any obvious sample widening during rolling
 90 [26].

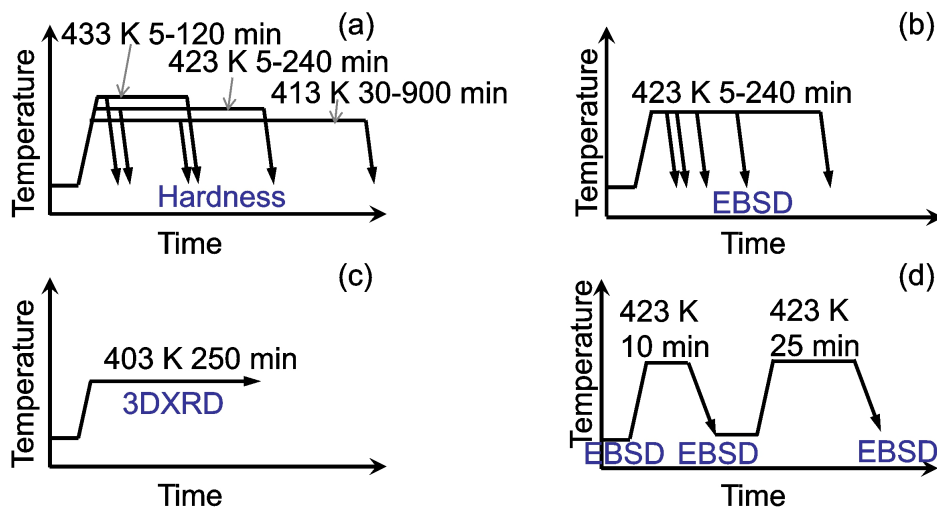
Table I: Chemical composition (weight percentage) of the material.

Cu	Ni(%)	Mg(%)	Al(%)
Balance	0.002	0.002	0.002

92 2.2 Vickers hardness test

93 Samples from the 90% cold-rolled plate were isothermally annealed in an air furnace at 413 K, 423 K and
 94 433 K for various time periods (Figure 1a). The microhardness of each annealed sample was examined
 95 using a Struers DuraScan fully automatic Vickers hardness tester. A load of 200 g was applied for 10 s
 96 during the tests.

Fig. 1: Sketches showing the thermal treatments on the 90% cold-rolled plate. (a) Annealing for hardness tests; (b) Annealing for post-mortem EBSD characterizations; (c) Annealing for in-situ 3DXRD measurements; (d) Annealing for ex-situ EBSD characterizations.



97 2.3 Post-mortem EBSD characterization for kinetics analysis

98 The 90% cold-rolled sample was isothermally annealed at 423 K for time periods from 5 min to 240 min
99 (see Figure 1b). This heat treatment results in samples with recrystallized volume fractions between 5%
100 and 95%, which are used for kinetics analysis.

101 The microstructures of the partially recrystallized samples were characterized using EBSD with a
102 step size of 1 μm on the longitudinal sections (defined by the rolling direction (RD) and the normal
103 direction (ND)). For each sample, two EBSD scans from widely separated sample areas were carried
104 out, each covering an area of 300 μm by 300 μm .

105 The recrystallized grains in the partially recrystallized microstructures were identified automatically
106 from the EBSD data by the method described in [27] using the following three criteria: 1) misorientations
107 inside the recrystallized grains should be less than 1° ; 2) the equivalent circular diameter (ECD) of the
108 recrystallized grains should be larger than 3 μm ; 3) each recrystallized grain should be at least partially
109 surrounded (more than 6 pixels along the grain boundary) by high angle boundaries (HABs) to the
110 deformed matrix, where HABs are defined as boundaries with misorientation angles larger than 15° . In
111 copper samples, annealing twins are common. In this work, if not stated otherwise, all twin boundaries
112 (maximum 2° deviation from the exact 60° $\langle 111 \rangle$ twin relationship) were ignored during reconstruction
113 of the recrystallized grains. In other words, a parent grain and all of its twins were considered as a unity.

114 We determined the following microstructural parameters for the analysis: the recrystallized volume
115 fraction (V_V), the interfacial area between the recrystallized grains and the deformed matrix per unit
116 volume (S_V), the number of recrystallized grains per unit volume (N_V), the Cahn-Hagel boundary mi-
117 gration velocities (G_{C-H}), and the contiguity ratio (C_{RexRex}). The contiguity ratio is a measure of the
118 fraction of impinging recrystallizing boundaries among all the recrystallizing boundaries. Stereological
119 principles were applied to deduce these volumetric parameters based on parameters determined from
120 2D characterizations using the following equations [28]:

$$V_V = A_{\text{Rex}}/A_{\text{Total}} \quad (2)$$

$$S_V = 4L_{\text{RexDef}}/\pi A_{\text{Total}} \quad (3)$$

$$N_V = 16V_V/9\pi D^3 \quad (4)$$

$$G_{C-H} = (dV_V/dt)/S_V \quad (5)$$

$$C_{\text{RexRex}} = 2S_{V,\text{RexRex}}/(2S_{V,\text{RexRex}} + S_V) \quad (6)$$

$$S_{V,\text{RexRex}} = 4L_{\text{RexRex}}/\pi A_{\text{total}}$$

125 where A_{Rex} is the area of all the recrystallized grains, A_{Total} is the total area of the characterized region,
126 L_{RexDef} and L_{RexRex} are the total length of the interface between recrystallized grains and the deformed
127 matrix, and between two recrystallized grains, respectively, D is the average linear intercept length of the
128 recrystallized grains, dV_V/dt is the time derivative of the recrystallized volume fraction, and $S_{V,RexRex}$
129 is the interfacial area per unit volume between two recrystallized grains.

130 2.4 3DXRD in-situ measurement

131 The 3DXRD experiments were conducted at the beamline P07 at PETRAIII, Deutsches Elektronen-
132 Synchrotron (DESY) using monochromatic X-rays of 50 keV. The sample for the 3DXRD in-situ measure-
133 ment was cut from the cold-rolled plate and electropolished to avoid nucleation from surface imperfec-
134 tions. The volume illuminated by X-rays was about $500 \times 500 \times 750 \mu\text{m}^3$. During the measurements,
135 an X-ray transparent furnace with an inert gas atmosphere was used to anneal the sample at 403 K (see
136 Figure 1c). During annealing, the sample was rotated around its vertical axis from $\omega = 0^\circ$ to $\omega = 30^\circ$
137 by sweeping intervals of 0.5° , while diffraction images were acquired at the same time. Each 30° sweep
138 took 5.7 min, which was hence the time resolution of the present experiment. The annealing tempera-
139 ture of 403 K was chosen to be lower than that used for the post-mortem investigations, so that the time
140 resolution of 5.7 min was significantly shorter than the time needed for full recrystallization, and thus
141 it became possible to follow the growth of individual grains in-situ with this time resolution. In total 42
142 sweeps were conducted, and the entire measurement took about 250 min.

143 Before annealing, the diffraction images were composed of Debye-Scherrer rings from the deformed
144 matrix. During annealing, diffraction spots from recrystallized grains appeared when the Bragg con-
145 dition was fulfilled. The intensities of the diffraction spots are a linear function of the volume of the
146 recrystallized grains, and the volumes of the recrystallized grains were determined using the method
147 described in the supplementary material of [29]. The diffraction spot of a particular recrystallized grain
148 was first identified from a diffraction image collected during the last 30° sweep, and then traced back
149 to the diffraction images from earlier sweeps. Diffraction from 8 crystal planes ($\{111\}$, $\{200\}$, $\{220\}$,
150 $\{311\}$, $\{222\}$, $\{400\}$, $\{331\}$, $\{420\}$) was recorded. For a grain with twins the $\{111\}$, $\{220\}$ and $\{222\}$
151 diffraction spots contain contributions from the grain itself plus some, but not all of the twins. In this
152 work, we therefore only used the $\{200\}$ and $\{400\}$ diffraction spots to avoid partially including twin
153 volumes. Each growth curve thus reflects the growth of one grain without its twins.

154 2.5 Ex-situ EBSD characterization

155 Ex-situ EBSD measurements were performed on one sample after different intervals of annealing. First,
156 the deformed microstructure on the longitudinal section was characterized using EBSD with a step size
157 of 0.1 μm . Two annealing steps were performed: a first step at 423 K for 10 min, and a second at the
158 same temperature for an extra 25 min (Figure 1d). For each annealing step, the sample was enclosed
159 in a vacuum glass tube with 50 kPa Ar (purity 99.999%). After each annealing step, the sample was
160 remapped using EBSD at the same surface location.

161 A slight misalignment of the EBSD maps before and after annealing was observed. This misalign-
162 ment was corrected using an affine transformation [30] with reference to the map after the second an-
163 nealing step.

164 The stored energy in the deformed microstructure was estimated by summing the energies of all
165 boundaries within the area of interest using the method introduced in [31]. The boundary energy per
166 unit area was calculated using the Read-Shockley equation:

$$\gamma = \begin{cases} \gamma_m(\theta/\theta_m)(1 - \ln(\theta/\theta_m)), & \text{if } \theta \leq \theta_m \\ \gamma_m, & \text{if } \theta > \theta_m \end{cases} \quad (7)$$

167 where γ_m is the energy per unit area of a high angle boundary, θ is the boundary misorientation, and
168 θ_m is the misorientation angle above which γ is independent of the misorientation angle. In this work,
169 we used $\gamma_m=0.625 \text{ J/m}^2$, and $\theta_m=15^\circ$. All boundaries with misorientation angles larger than 2° were
170 taken into account in the calculation of the stored energy. To visualize the local variation of the stored
171 energy, we calculated for each pixel of an EBSD map the stored energy density in a square region of
172 $0.7 \times 0.7 \mu\text{m}^2$ around this pixel. It is noted that the stored energy determined by this method only
173 includes dislocations that contribute to dislocation boundaries with misorientation angles larger than
174 2° , and the method will thus tend to underestimate the stored energy.

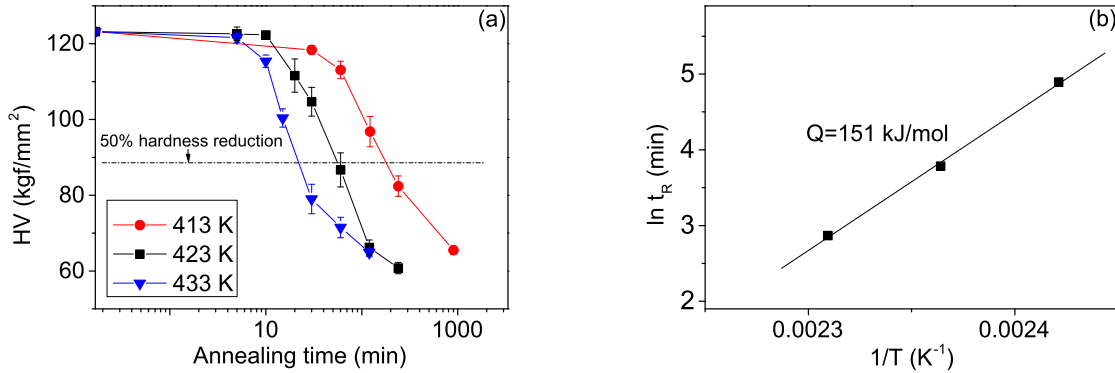
175 3 Results

176 3.1 Recrystallization kinetics

177 3.1.1 Recrystallization kinetics determined by hardness

178 The decrease in hardness as a function of annealing time is shown in Figure 2a for temperatures from
 179 413 K to 433 K. The estimated time corresponding to 50% hardness reduction (i.e. the hardness value
 180 equals to $(HV_{Def} + HV_{Rex})/2$, where HV_{Def} and HV_{Rex} are the hardness in the deformed and fully
 181 recrystallized state, respectively) is used as the characteristic recrystallization time (t_R) at each temper-
 182 ature. Figure 2b shows the dependence of $\ln(t_R)$ on $1/T$. For the present data, an activation energy
 183 Q of 151 kJ/mol is found using the Arrhenius equation. In spite of the narrow temperature interval
 184 used here, which means that the accuracy in determination of Q is limited, it is satisfying to notice that
 185 the observed value of 151 kJ/mol is well within the range of Q values from 85 kJ/mol to 170 kJ/mol,
 186 reported for 3N copper (purity >99.9%) [32].

Fig. 2: (a) Vickers microhardness as a function of time for annealing at three temperatures. The error bars show the standard error of the mean for measurements on the same sample. (b) Temperature dependence of t_R , where t_R is the time for 50% hardness reduction.

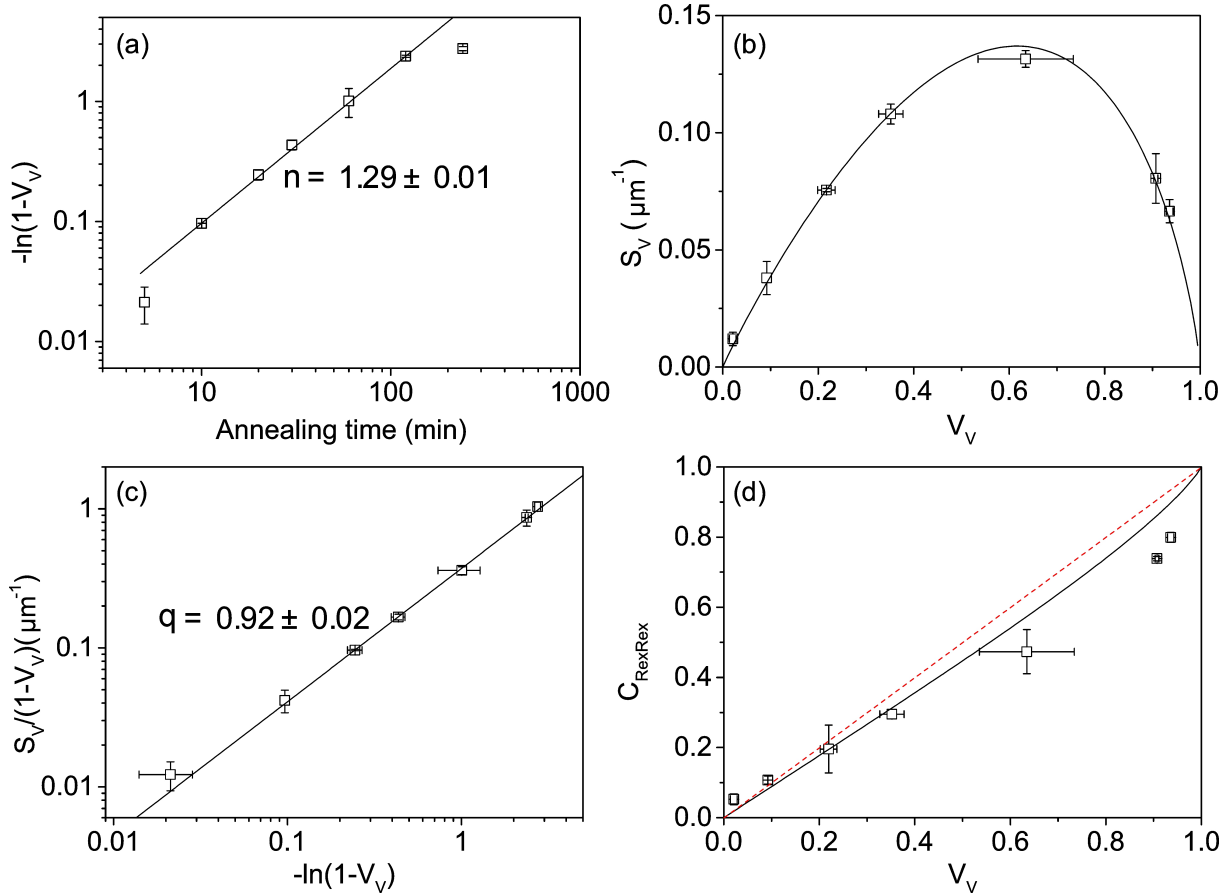


187 3.1.2 Evolution of V_V and S_V during isothermal annealing at 423 K

188 The recrystallized volume fraction during isothermal annealing at 423 K was determined from the EBSD
 189 measurements, and is shown as a function of time in an Avrami plot in Figure 3a, i.e. $-\ln(1 - V_V)$ vs. t
 190 on a $\log_{10} - \log_{10}$ scale. For idealized JMAK kinetics (Eq. 1), all the data points should follow a straight
 191 line, with a slope corresponding to the Avrami exponent n . For the present data, a straight line can
 192 be fitted to the points corresponding to annealing times from 10 min to 120 min, whereas data points
 193 outside this range show obvious deviations. The slope of the fitted line is 1.29, which is much lower than

194 the expected 3 to 4 in the idealized JMAK model. An Avrami exponent around 1 is, however, frequently
 195 reported for copper [32], and also for other metals, e.g. steel [33] and Mg [34].

Fig. 3: Evolution of the recrystallized volume fraction (V_V), the interfacial area between recrystallized grains and the deformed matrix per unit volume (S_V), and the contiguity ratio C_{RexRex} . (a) Avrami plot showing $-\ln(1 - V_V)$ as a function of annealing time in a double logarithmic plot. (b) S_V as a function of V_V . (c) VMR path plot: $S_V/(1 - V_V)$ vs. $-\ln(1 - V_V)$ in a double logarithmic plot. A solid line is fitted in (c), from which the values of q and C in Eq. 8 are determined. In turn, these q and C values are used to calculate the curve shown in (b). (d) Contiguity ratio C_{RexRex} vs. V_V . The solid line in (d) shows the analytical prediction for random nucleation, and the dashed line represents $C_{\text{RexRex}} = V_V$.



196 S_V represents the area of recrystallizing boundaries per unit volume that have not impinged upon
 197 other recrystallized grains, i.e. boundaries free to migrate. Figure 3b shows the evolution of S_V as a
 198 function of V_V . An interesting feature in Figure 3b is that the peak occurs at a V_V higher than 0.5. The
 199 peak of S_V is expected to appear at $V_V \approx 0.5$ for random nucleation [35]. When clustered nucleation oc-
 200 curs, recrystallized grains tend to impinge upon each other earlier, and the peak of S_V will shift towards
 201 lower values of V_V , as shown experimentally for aluminium [36] and in analytical and numerical simu-
 202 lations [37, 38]. A shift of the peak towards higher V_V is not so often reported, but Jäggle and Mittemeijer
 203 [32] reported a very similar shift in a cross-rolled pure copper sample.

204 For the dependence of S_V on V_V , Vandermeer et al. [15] suggested a path function:

205

$$S_V = C(1 - V_V)(-\ln(1 - V_V))^q \quad (8)$$

206 using two parameters, C and q . With Eq. 8, it is deduced that q larger than 0.69 corresponds to a shift
 207 of the peak of the S_V - V_V curve towards V_V larger than 0.5. In Figure 3c, we plot $S_V/(1 - V_V)$ vs.
 208 $-\ln(1 - V_V)$ on a $\log_{10} - \log_{10}$ scale in a so-called VMR path plot, and fit the data points to a straight
 209 line. With linear regression, we find $q = 0.96$ and $C = 0.37\mu\text{m}^{-1}$. These parameters are related to the
 210 growth and nucleation conditions, which will be discussed in Section 4.1.

211 3.1.3 Spatial distribution of the recrystallized grains

212 The contiguity ratio (C_{RexRex}) is a parameter relevant to detect microstructural deviations from nucle-
 213 ation at random sites [39, 40]. When plotting C_{RexRex} as a function of V_V , a straight line connecting
 214 the points (0,0) and (1,1) is often considered to describe random nucleation (the dashed red line in Fig-
 215 ure 3d), but according to [41], the correct theoretical expression for the random nucleation case has a
 216 more sophisticated analytical form, which is represented by the solid black curve in Figure 3d. If nu-
 217 cleation is clustered, points will be above the curve (e.g. [42]). Points below the curve appear when
 218 nucleation occurs in an ordered way: for example, if the nuclei are ordered in a simple cubic lattice,
 219 C_{RexRex} will be zero until V_V reaches a certain value given by the distance between the nuclei [39].

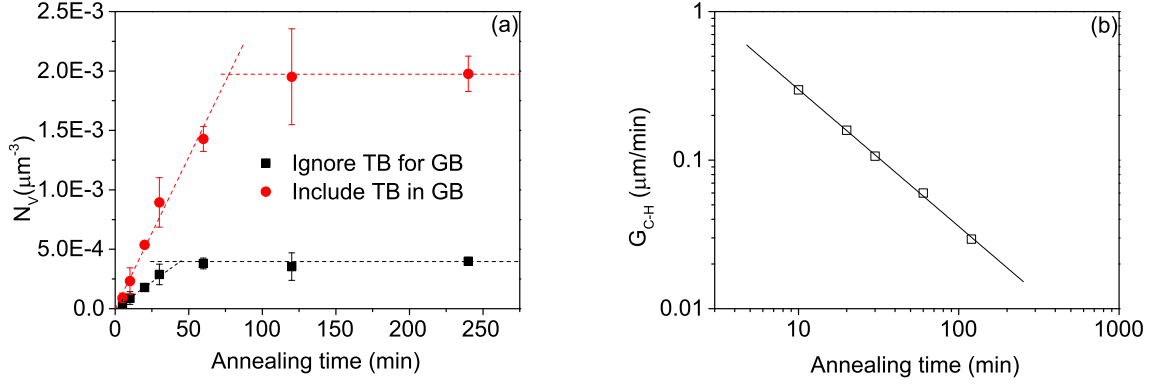
220 The contiguity ratio C_{RexRex} for the present sample follows approximately the curve for random
 221 nucleation for $V_V < 0.5$. Data points for $V_V > 0.6$ tend to be below the curve (see Figure 3d). This
 222 suggests that regions which are hard to recrystallize may be distributed in an ordered manner.

223 3.1.4 Nucleation rates and recrystallizing boundary velocities

224 The number of recrystallized grains per unit volume (N_V) is plotted as a function of annealing time in
 225 Figure 4a. When a grain and its twins are counted as one grain, N_V increases linearly with annealing
 226 time until approximately 50 min ($\sim 60\%$ recrystallized), after which N_V saturates. When twins are
 227 counted as separated grains, N_V increases linearly until approximately 80 min ($\sim 80\%$ recrystallized).
 228 In both cases, dN_V/dt is almost constant before saturation, which means that the nucleation rate $\dot{N} =$
 229 $(dN_V/dt)/(1 - V_V)$ [43] is approximately constant before saturation is reached. Extrapolating the data
 230 points in Figure 4a to $t = 0$ results in N_V close to 0. Therefore, the nucleation condition for the sample
 231 can be described as nucleation with a constant rate until saturation is reached.

232 To determine the Cahn-Hagel boundary migration velocity (G_{C-H}) using Eq. 5, dV_V/dt is derived

Fig. 4: Nucleation and growth results. (a) Number of recrystallized grains per unit volume N_V as a function of annealing time. Annealing twin boundaries (TB) are either ignored or included as normal grain boundaries (GB) when determining the intercept length of the recrystallized grains D , which are used in Eq. 4 to determine N_V . When twin boundaries are ignored, a grain and all of its twins are counted as one grain, otherwise twins are counted as separated grains. (b) Cahn-Hagel boundary migration velocity (G_{C-H}) as a function of annealing time. The fitted solid line in (b) has a slope of -0.92 ± 0.02



233 from the JMAK equation (Eq. 1):

$$dV_V/dt = kn \exp(-kt^n) t^{n-1} \quad (9)$$

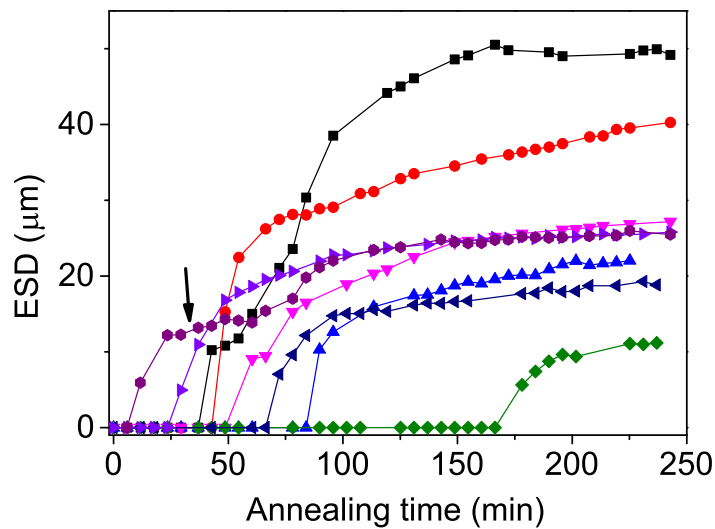
234 where the values of $k = 5 \times 10^{-3} \text{ min}^{-1.29}$ and $n = 1.29$ are obtained by fitting the data points in
 235 Figure 3a. The recrystallized volume fractions for 5 min and 240 min annealing time do not follow
 236 the straight line in Figure 3a. They are therefore not included in determination of the time derivative
 237 dV_V/dt . Figure 4b shows the evolution of G_{C-H} as a function of t on a $\log_{10} - \log_{10}$ scale. The data
 238 points can be fitted by a straight line with a slope of -0.92, which means that G_{C-H} decreases as $t^{-0.92}$ in
 239 the selected time interval (10 min to 120 min).

240 3.2 Growth of individual grains measured by 3DXRD

241 We followed the growth of 835 individual recrystallized grains in-situ. The growth curves of eight
 242 individual grains are shown in Figure 5 representing the equivalent sphere diameter (ESD) as a function
 243 of time. The growth curves vary from grain to grain, which is similar to measurements for aluminium
 244 [16, 17]. For 3DXRD results, the growth rate is defined as the increase of ESD per unit time. We do not
 245 observe a linear increase in ESD for any of the growth curves, i.e. no grain follows the idealized JMAK
 246 assumption of growth at a constant rate. Instead, most of the grains show a fast growth stage for a
 247 limited time period after nucleation, after which the growth rate decreases quickly, reaching a stagnation
 248 period. Only very few grains, like the one with the growth curve marked by an arrow, continue to grow
 249 again after a stagnation period. The other grains just stop growing or grow only very slowly after
 250 reaching the stagnation period. If we use the ESD of each grain at the end of the in-situ measurement
 251 as the stagnation size, the recrystallized grains reaches 80% of their stagnation size on average after

252 61 min. One may speculate whether impingement between the recrystallized grains may explain this
 253 stagnation. Using the calculated activation energy $Q = 151$ kJ/mol (Figure 2b), it is found that the time
 254 to reach 50% recrystallization at 403 K is expected to be 370 min. This means that stagnation time in the
 255 order of 61 min is significantly shorter than t_R . Thus the influence of impingement between different
 256 recrystallized grains during the monitored 250 min is not significant, and the observed stagnation can
 257 therefore not be explained by impingement for the present sample. This is further documented by the
 258 ex-situ electron microscopy characterization (see Section 3.3).

Fig. 5: Increase of the equivalent sphere diameter (ESD) of individual grains as a function of annealing time, measured by 3DXRD during in-situ annealing at 403 K. The arrow marks the growth curve of a grain that continues to grow again after a stagnation period.

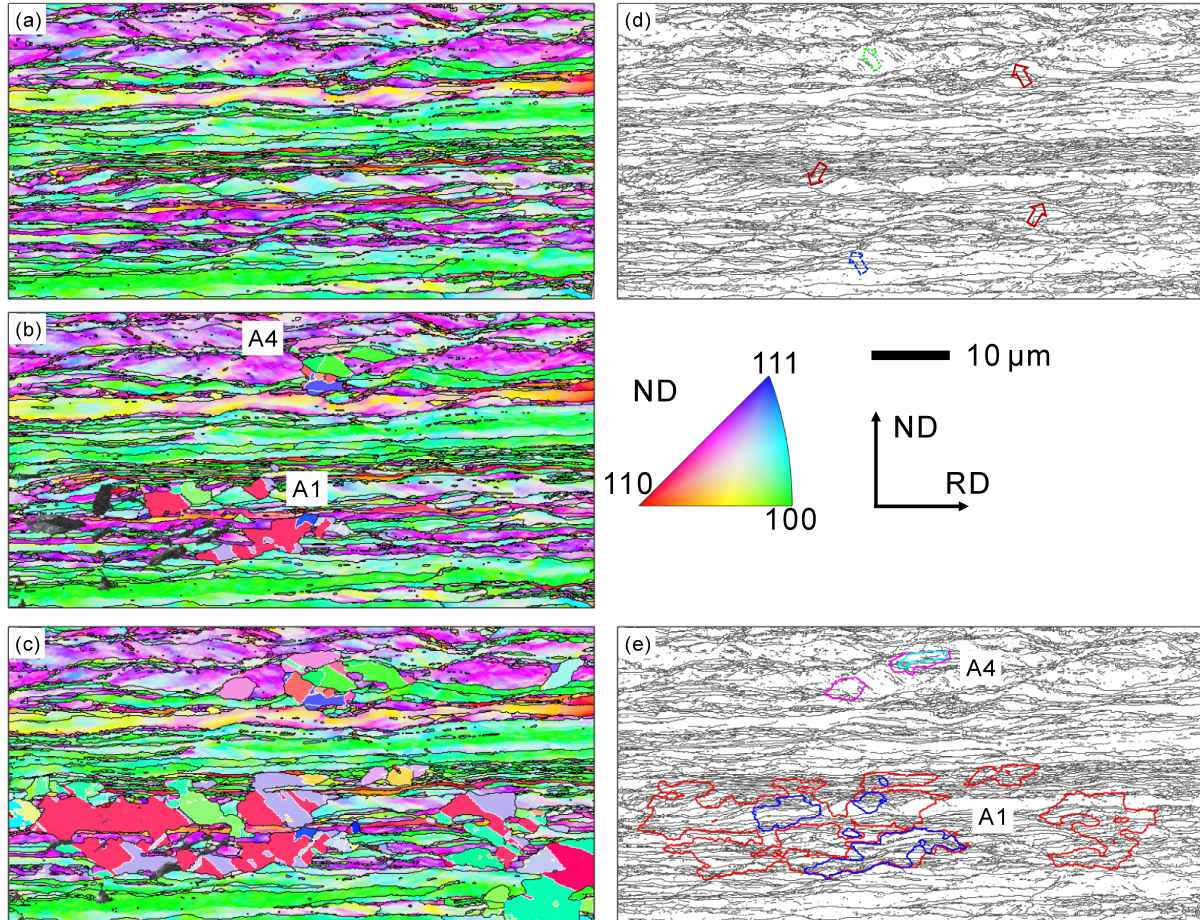


259 3.3 Ex-situ measurement of migration of recrystallizing boundaries

260 To further investigate why most grains only have a short period of fast growth followed by stagnation
 261 or very slow growth, an ex-situ EBSD experiment was conducted. Figure 6a-c shows EBSD maps of the
 262 same area in the deformed state and after 10 min and 35 min annealing at 423 K. It is noted that the
 263 area fraction of recrystallized grains on the observed surface is only around 0.1 after 35 min annealing,
 264 less than that in a bulk sample as reported in Section 3.1.2. This is not surprising, as the sample is semi-
 265 bulk. This means that only nuclei underneath the surface can grow into the characterized surface and
 266 contribute to the recrystallized area, whereas in real bulk samples, as those used for the post-mortem
 267 analysis, nuclei from both sides will grow into the characterized surfaces.

268 Before annealing, the deformed microstructure is composed of bands with different crystallographic
 269 orientations (Figure 6a). Most of the bands are approximately parallel to RD. Localized shear bands,

Fig. 6: Growth of individual grains during ex-situ annealing at 423 K. (a)-(c) Orientation maps in the deformed state (a) and after 10 min (b) and 35 min (c) annealing. Boundaries with misorientations larger than 5° are shown in black. Twin boundaries are shown in white. (d) Boundaries with misorientation larger than 5° within the deformed microstructure before annealing. Localized shear bands are marked by arrows. (e) Contours of two recrystallized grains (A1 and A4) after 10 min and 35 min are shown on top of the boundary map of the deformed microstructure.



270 inclined approximately $\pm 35^\circ$ to RD, are also observed (marked by arrows in Figure 6d). The deformed
 271 sample has a typical rolling texture, consisting of 16% copper ($\{112\} \langle 111 \rangle$), 19% brass ($\{110\} \langle 112 \rangle$) and
 272 42% S ($\{123\} \langle 634 \rangle$) orientations, within a maximum 15° deviation from the ideal texture components.

273 Four grains were observed after 10 min annealing. In this work, we focus on the two grains termed
 274 A1 and A4 (see Figure 6b), because these two grains are entirely unimpinged after the first annealing
 275 step. Due to twinning, each grain contains several parts with different orientations. Moreover, both
 276 grains contain parts that are not connected in 2D: the unconnected parts are composed of regions with
 277 identical orientations (misorientation $< 1^\circ$). For illustration, the recrystallizing boundaries of the two
 278 grains are superimposed on top of the deformed structure in Figure 6e. The overall shape of grain A1
 279 is elongated along RD, whereas near the shear band marked by the dashed (blue) arrow in Figure 6d,
 280 a part of the grain appears to be elongated along the shear band direction. The two parts of grain A4

281 appear to align along the direction of the shear band marked by the dotted (green) arrow in Figure 6d.

282 From Figure 6e, it is seen that different segments of the recrystallizing boundaries move with differ-
 283 ent velocities, i.e. exhibit non-uniform growth, and some unimpinged segments are almost stationary.
 284 Considering the accuracy of alignment between different EBSD maps, a boundary segment is considered
 285 stationary, if it shows a displacement less than 2 pixels ($0.02 \mu\text{m}$) during the second annealing step. This
 286 is more clearly shown in Figure 7, where the stationary boundary segments are highlighted in green. For
 287 grain A1, 33% of the unimpinged boundary segments are stationary during the second annealing step.
 288 This fraction is 32% for grain A4. These stationary boundaries and those moving very slowly contribute
 289 to a decrease in the average boundary migration velocity.

Fig. 7: Sketch showing the recrystallizing boundary positions for grains A1 and A4.

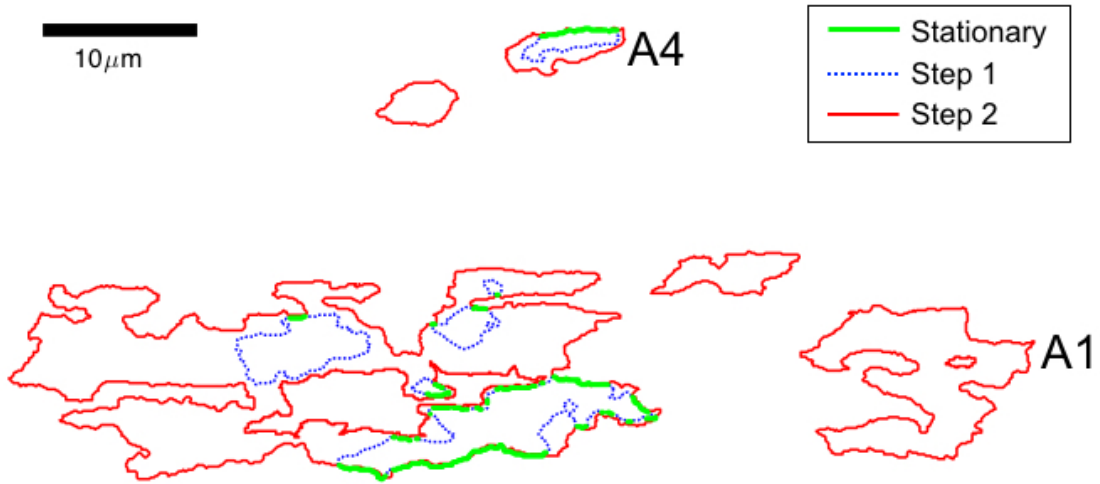


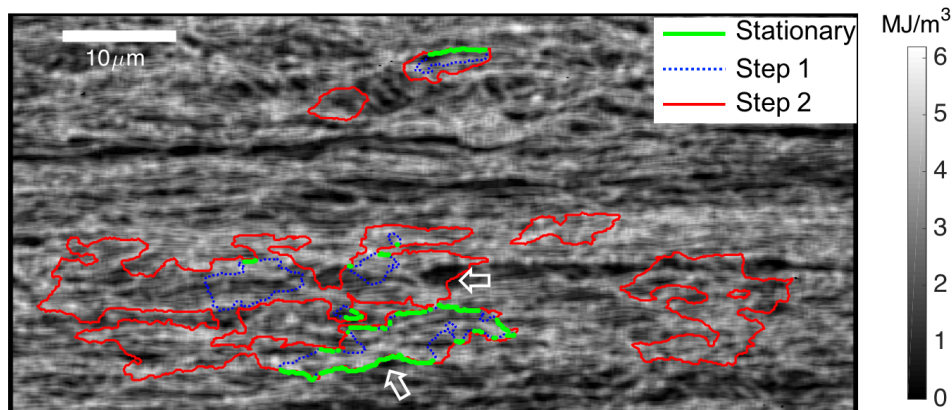
Table II: Grain areas and average stored energy density. $E_{s,mig}$ is the average stored energy density within the area that the migrating boundaries sweep during each annealing step. $E_{s,sta}$ is the average stored energy density in the area ahead of the stationary boundaries.

	Grain A1			Grain A4		
	Area (μm^2)	$E_{s,mig}$ (MJ/m^3)	$E_{s,sta}$ (MJ/m^3)	Area (μm^2)	$E_{s,mig}$ (MJ/m^3)	$E_{s,sta}$ (MJ/m^3)
Step 1 (0-10 min)	81.5	3.3		7.0	2.7	
Step 2 (10-35 min)	392.2	3.1	2.7	25.3	2.9	3.1

290 With the present ex-situ data, it is possible to analyze the deformed microstructure invaded by the
 291 recrystallized grains. Similar analysis was performed in [44]. We can thus test, if the stored energy
 292 and/or misorientation across the boundaries may explain why some boundaries are stationary while
 293 others migrate. Figure 8 shows the local variations of the stored energy density (E_s) determined from
 294 the EBSD map before annealing. The local E_s varies from 0.5 to $6.2 \text{ MJ}/\text{m}^3$, and the average E_s of this
 295 map is $2.8 \text{ MJ}/\text{m}^3$. For both grains A1 and A4, the invaded regions include regions of high and low E_s .
 296 Similarly both high and low E_s regions are observed next to the stationary boundaries (see Figure 8).

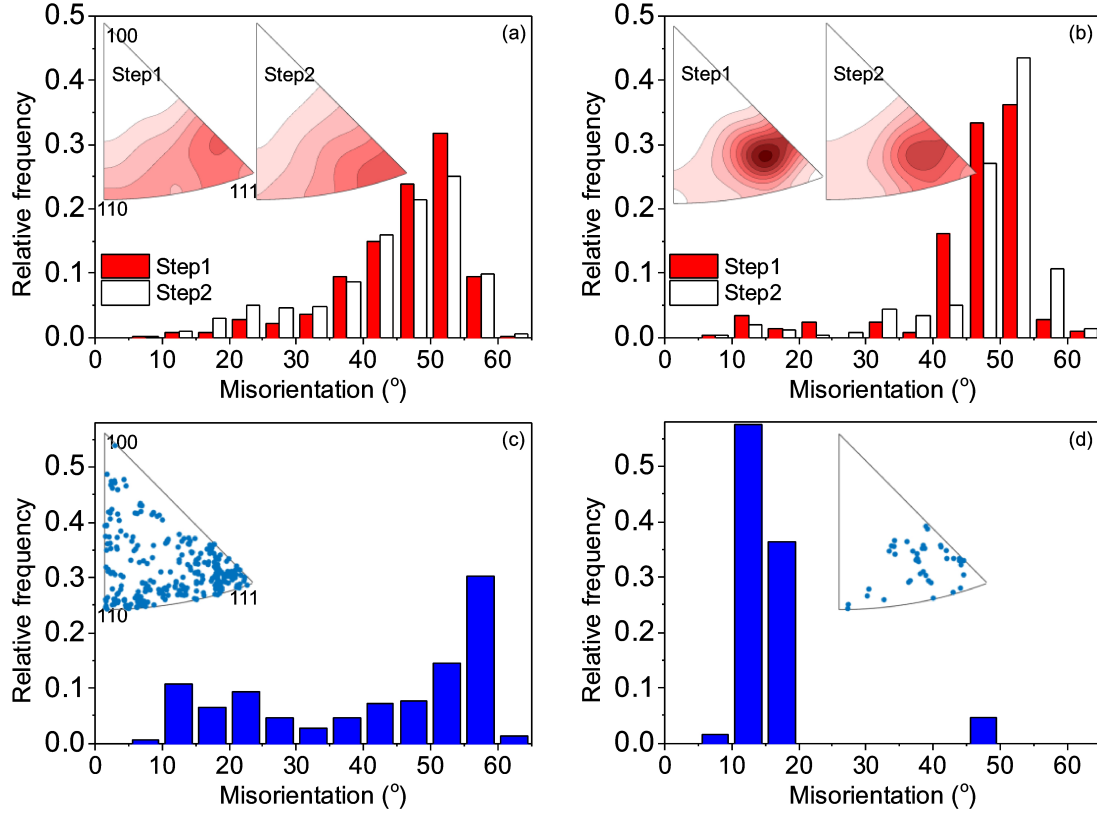
297 For a quantitative analysis, we determined an average E_s ahead of the stationary boundaries consider-
 298 ing regions within $2\ \mu\text{m}$ to the stationary boundaries, noted as $E_{s,sta}$. The average stored energy density
 299 within the invaded region, i.e. the area that the migrating boundaries sweep during the annealing step,
 300 is noted as $E_{s,mig}$. As listed in Table II, the average E_s ahead of the stationary boundaries is similar to
 301 those invaded by the migrating boundaries, and the average $E_{s,mig}$ for the migrating boundaries are
 302 similar during the first and the second annealing steps. For the deformed matrix remaining unrecrys-
 303 tallized after the second annealing step, the stored energy density can be calculated not only from EBSD
 304 maps before annealing, but also from maps after each of the first and the second annealing steps, which
 305 are $2.9\ \text{MJ}/\text{m}^3$, $2.9\ \text{MJ}/\text{m}^3$ and $2.7\ \text{MJ}/\text{m}^3$, respectively. This shows that recovery of the deformed ma-
 306 trix is very limited during the present annealing, which is consistent with other observations reported
 307 in literature for copper [45].

Fig. 8: Stored energy density map. The local store energy density is represented in gray scale. The
 recrystallizing boundaries of grains A1 and A4 after the first and the second annealing steps, and the
 stationary boundaries are also shown. Two low E_s regions ahead of the stationary boundaries or invaded
 by the recrystallized grains are indicated by arrows.



308 For each pixel in the recrystallized grains, we calculate the misorientation between this pixel and the
 309 orientation at the same location in the EBSD map before annealing. With this method, we determined
 310 the distribution of misorientations to the invaded deformed microstructure during each of the first and
 311 second annealing steps (Figure 9a and b). For both grains, the distributions of the misorientation angles
 312 peak at 50° - 55° with a misorientation axis close to $\{111\}$. The distributions of misorientations are not
 313 significantly different between the first and the second annealing steps. The misorientations across the
 314 stationary boundaries are plotted in Figure 9c and d. The peak of the misorientation angles is shifted to
 315 55° - 60° for grain A1, whereas for grain A4, more than half of the misorientation angles are less than 15° .

Fig. 9: Distributions of misorientations between the recrystallized grains A1 (a) and A4 (b) and the invaded deformed regions during the two annealing steps, and distributions of misorientations across stationary recrystallizing boundaries for grains A1 (c) and A4 (d).



316 4 Discussion

317 4.1 Avrami exponent and shift of the peak of the S_V-V_V curve

318 The Avrami exponent n depends on both the nucleation and growth conditions. Vandermeer et al [15]
 319 proposed a model for transformation using the assumptions of random nucleation and shape preserved
 320 growth. In their model, the nucleation rate \dot{N} and the average boundary migration velocity G of the
 321 recrystallized grains are expressed as:

$$322 \dot{N} = N_1 t^{\delta-1} \quad (10)$$

$$323 G = r P t^{r-1} \quad (11)$$

324 where t is the annealing time, and N_1 , δ , r and P are parameters describing the nucleation and growth
 325 conditions. The Avrami exponent n is then equal to $\delta + 3r$. The post-mortem kinetics analysis of this
 326

327 sample shows that the average boundary migration velocity G_{C-H} has a time dependence of $t^{-0.92}$
 328 (see Figure 4b), which according to Eq. 11 gives a very small r of 0.08. Considering that the constant
 329 nucleation rate observed experimentally leads to a δ of 1 according to Eq. 10, the model would predict
 330 an Avrami exponent close to the experimentally observed value of 1.29 (Figure 3a).

331 In the model of Vandermeer, the fitting parameter q of the VMR path function Eq. 8 can also be re-
 332 lated to the nucleation and growth conditions using the following equation [15]:

333

$$q = \frac{2r + \delta}{3r + \delta} \quad (12)$$

334 For our sample we find from Figure 3c a q of 0.96. According to Eq. 12, the upper limit of q is 1, which oc-
 335 curs when $\delta \gg r$. For the present sample, the decreasing average growth rate of the recrystallized grains
 336 with $r = 0.08$ in combination with a constant nucleation rate can rationalize q being approximately 1. An
 337 understanding why the average growth rate of the recrystallized grains/average migration velocity of
 338 the recrystallizing boundaries decreases so strongly is therefore essential for the present recrystallization
 339 kinetics.

340 4.2 Decreasing boundary migration velocities

341 As revealed by the in-situ 3DXRD measurement, most grains approach stagnation after a short period of
 342 fast growth. The occurrence of such behavior was proposed in [46]. This particular growth behavior can
 343 be used to explain the decrease of G_{C-H} with increasing time. Considering the extreme case that each
 344 recrystallized grain will reach its stagnation size immediately after nucleation, G_{C-H} will decrease as a
 345 function of t^{-1} (see Appendix). In other words, the measured average boundary velocities will show a
 346 time dependence close to t^{-1} , if the growth period for individual grains is very short. For many other
 347 materials, measured average boundary velocities are reported to have a time dependence of $t^{-\alpha}$ with α
 348 close to 1 (e.g. [12, 13, 35]), which may thus be due to fast growth to a stagnation size, as in the present
 349 sample.

350 This fast growth to a stagnation size can be attributed to non-uniform boundary migration veloci-
 351 ties, as revealed by the ex-situ EBSD measurements. Among the unimpinged recrystallizing boundaries,
 352 some boundary segments migrate fast, whereas others have low migration velocities or even become
 353 stationary. However, fast moving boundaries will not migrate forever with high velocities, they will
 354 either impinge upon other recrystallized grains, or slow down when entering a deformed region un-
 355 favorable for grain boundary migration. As slowly moving boundaries will not migrate much further,
 356 they will be preserved for an extended time period, and the fraction of slowly moving boundaries will

357 thus increase with increasing annealing time. Due to this accumulation of stationary boundaries, recrystallized grains will reach a stagnation size without full impingement upon other recrystallized grains. 358
359 G_{C-H} is the average migration velocity of all the unimpinged boundaries, and as the fraction of slowly moving boundaries increase with annealing time, G_{C-H} will decrease correspondingly even though fast 360 migrating boundaries appear when new nuclei form. 361

362 The classic equation for boundary migration velocity is expressed as [47]:

$$G = MF \quad (13)$$

363 where M and F are the boundary mobility and driving force, respectively. The stored energy within the deformed matrix provides driving force for recrystallization. Decrease of the stored energy with increasing annealing time due to recovery of the deformed matrix (e.g. [5]) or variations of local stored energy (e.g. [4, 48–51]) has been frequently used to explain the decrease of the average boundary migration velocity during annealing. Our quantitative analysis based on the ex-situ characterization shows 364 that after two steps of annealing, the recovery of the deformed matrix is very minor, which excludes the possibility of concurrent recovery for slowing down boundary migration. Variations of local stored energy are present in this sample. Conventionally, it is argued that the high E_s regions will be invaded 365 first, leaving lower E_s regions to be invaded in the following steps. Our results, however, do not agree with this stipulation. Although a few stationary boundary segments seem to stop at a local region with 366 low stored energy (see Figure 8), the average value of E_s ahead of the stationary boundaries is not significantly different from that of the invaded regions (Table II). Therefore, neither the reduction in stored energy due to recovery nor variations of local stored energy are the main reasons leading to stationary 367 boundaries for the present sample. 368
369
370
371
372
373
374
375
376

377 The boundary mobility is the other factor determining the boundary migration velocities. The analysis of the ex-situ results shows that misorientations of stationary boundaries are quite different from 378 those of migrating boundaries (Figure 9). The majority of stationary boundaries of grain A4 has misorientations less than 20° . It is well recognized that low angle boundaries (LABs) have low mobility, 379 which will lead to the so-called "orientation pinning" effect [13, 52]. The stationary boundary segments observed for grain A4 can be explained by orientation pinning. For grain A1, the stationary boundaries 380 tend to have a large fraction of misorientations larger than 55° , but only approximately 6% of these misorientations are within $15^\circ/\sqrt{3}$ to the ideal twin relationship, and thus an explanation based solely 381 on twins is not appropriate. The dependences of the boundary mobility on the misorientation are very complex [53], and also depend on the boundary plane [54]. With the present 2D ex-situ data, crystallographic planes of the boundaries are unknown, and thus no further analysis of the boundary plane 382
383
384
385
386
387

388 effects is possible with the present data.

389 Another reason for why some boundaries become stationary or migrate only very slowly may be
390 related to the morphology of the deformed microstructure. Recent 3D studies have shown that the local
391 geometrical arrangement of the dislocation boundaries has a strong influence on the local boundary
392 migration [55, 56]. Migration of recrystallizing boundaries which are perpendicular to the dislocation
393 boundaries are favored. A similar trend is seen in the present sample. In this cold-rolled sample, most
394 of the high angle boundaries are lamellar boundaries parallel to RD. The ex-situ annealing EBSD results
395 show that boundary segments parallel to ND have a tendency to move faster than those parallel to RD.
396 For recrystallizing grains near shear bands, the recrystallizing boundaries appear to migrate following
397 the shear band direction. It is thus suggested that the morphology of the deformed microstructure is
398 also important, and has to be considered when analyzing migration of the recrystallizing boundaries.

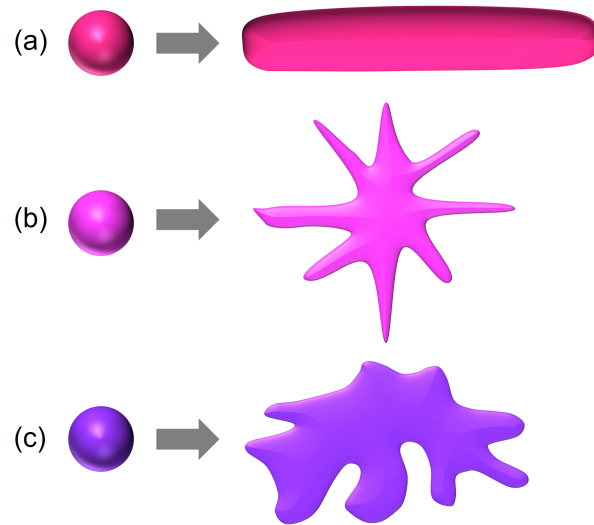
399 4.3 Growth dimensionality

400 In literature, a decrease in G_{C-H} as a function of annealing time has been suggested to be related to non-
401 3D/low-dimensional growth [57]. If recrystallized grains grow radially to form plates (2D growth) or
402 lengthen to form rods (1D growth), the G_{C-H} method will still average over the entire unimpinged grain
403 boundaries, and thus not describe the radial/lengthening migration rate well. In both the 1D and 2D
404 growth situations, G_{C-H} will show a decrease as t^{-1} at long annealing time even for a constant velocity
405 [57]. In other words, a low-dimensional growth will result in a similar decrease of the average bound-
406 ary migration velocity as observed here for non-uniform 3D growth. The concept of low-dimensional
407 growth has also been used to explain a low Avrami exponent. For example, for site saturated nucle-
408 ation, $n = 2$ for 2D growth with a constant radial growth rate, and $n = 1$ for 1D growth with a constant
409 lengthening rate [58]. For low-dimensional growth, the grain shape will change significantly during
410 growth: rods will become longer (1D growth) and plates will enlarge (2D growth) without changing
411 their thickness. For the present sample, this is not the case (see Figure 6).

412 The present non-uniform growth however has some similarities with non-3D growth, and may thus
413 be falsely interpreted as non-3D growth. Considering 1D growth, a grain will change from a sphere to a
414 rod, as shown in Figure 10a. If the growth occurs in 3D but highly non-uniform with stationary bound-
415 ary segments, the initial sphere will turn into a sea urchin shape (Figure 10b). This extreme case of non-
416 uniform growth is indeed another type of 1D growth, but with more than one lengthening direction. In
417 reality, depending on the difference in migration velocities of the fast and slowly migrating boundaries,
418 the growth is more or less like the case shown in Figure 10c, leading to grains with an amoeba shape.
419 As a consequence of the similarities between non-uniform 3D growth and low-dimensional growth, the

420 recrystallization kinetics may appear similar. Determination of whether the growth behavior is low-
421 dimensional or non-uniform thus requires analysis of more parameters than the Avrami exponent n ,
422 and it is necessary to check the shapes of the recrystallized grains in order to distinguish these two
423 situations. Grains with an amoeba shape in a partially recrystallized state are a strong indicator of non-
424 uniform growth. In literature, grains with an amoeba shape have also been reported for other metals,
425 such as Al [54, 59]. Recrystallization kinetics of these metals may also be determined by non-uniform
426 grain boundary migration, as suggested in this work.

Fig. 10: Sketch showing (a) low-dimensional, non-3D growth, (b) 3D growth with many stationary boundary segments, and (c) 3D growth with boundary segments migrating at different velocities.



427 5 Conclusions

428 We have investigated recrystallization kinetics of a polycrystalline copper sample cold-rolled to 90 % re-
429 duction in thickness, aiming at understanding why the sample has a low Avrami exponent and strongly
430 decreasing boundary migration velocities, which are observations frequently reported in literature for
431 many materials. The following conclusions are obtained:

- 432 1. The strongly decreasing average migration velocity of recrystallizing boundaries is the major reason
433 for the low Avrami exponent.
- 434 2. Migration velocities of the recrystallizing boundaries are non-uniform: different segments of the
435 boundaries have significantly different velocities; some continue to move while some become station-
436 ary. As the fraction of boundaries with low migration velocities accumulates during recrystallization,
437 this non-uniform boundary migration behavior leads to a decrease in the average velocity of the recryst-
438 allizing boundaries as a function of annealing time.
- 439 3. The non-uniform boundary migration behavior is related to the misorientations with the deformed

440 matrix, whereas effects of stored energy are less significant. It is further suggested that the local geomet-
 441 rical arrangement of the dislocation boundaries may affect boundary migration.

442 4. Non-uniform 3D growth may lead to recrystallization kinetics appearing similar to that for low-
 443 dimensional growth. Shapes of the recrystallized grains in a partially recrystallized state can be used to
 444 evaluate whether recrystallized grains exhibit low-dimensional or non-uniform growth.

445 Acknowledgements

446 FXL is mandated by the Belgian National Fund for Scientific Research (FSR-FNRS). The authors warmly
 447 thank Dr. R.A. Vandermeer for fruitful discussions on MPM. The authors also acknowledge beamtime
 448 by DESY under proposal number I-20110560 EC and Dr. N. Schell for assistance in using beamline P07.
 449 Dr. Hong Liu is thanked for help in preparation of the manuscript.

450 Appendix: Cahn-Hagel average boundary migration velocity for in- 451 stantaneously stagnated growth

452 Considering the extreme case that the growth rates of the individual grains can be described by a Dirac
 453 delta function at $t = t_{nucleation}$, each recrystallized grain will reach its stagnation size immediately after
 454 nucleation. The increase of V_V and S_V will thus be controlled by nucleation only. This can be analyzed
 455 further by using the idea of the extended interfacial area per unit volume $S_{V_{ext}}$ and the extended re-
 456 crystallized volume fraction $V_{V_{ext}}$, which are the fictive density of interfacial area and the fictive recryst-
 457 tallized volume fraction under the theoretical situation that grains are allowed to overlap. If the nuclei
 458 are randomly distributed in space, and their shapes are preserved, $V_{V_{ext}} = -\ln(1 - V_V)$, and $S_{V_{ext}} =$
 459 $S_V/(1 - V_V)$. The Cahn-Hagel boundary velocity can then be written as $G_{C-H} = (dV_{V_{ext}}/dt)/S_{V_{ext}}$. By
 460 expressing the nucleation rate \dot{N} using Eq. 10, the average G_{C-H} will be:

$$G_{C-H} = \frac{dV_V}{dt} \frac{1}{S_V} = \frac{dV_{V_{ext}}}{dt} \frac{1}{S_{V_{ext}}} = \frac{v_{Rex} \dot{N}}{s_{Rex} \int_0^t \dot{N} d\tau} = \frac{v_{Rex}}{s_{Rex}} \delta t^{-1} \quad (14)$$

461 where v_{Rex} and s_{Rex} are the average extended volume and average extended surface area of stagnated
 462 recrystallized grains, and both can be assumed to be independent of the annealing time. It is seen that
 463 in this extreme case, G_{C-H} will decrease as a function of t^{-1} .

References

- 464 [1] W. A. Johnson, R. F. Mehl: *Trans. Aime* 1939, vol. 135 (8), pp. 396–415.
- 465 [2] M. Avrami: *The Journal of Chemical Physics* 1939, vol. 7 (12), pp. 1103–1112.
- 466 [3] A. N. Kolmogorov: *Bull. Acad. Sci. USSR, Math. Ser* 1937, vol. 1, pp. 355–359.
- 467 [4] H. Luo, J. Sietsma, S. Van Der Zwaag: *Metallurgical and Materials Transactions A* 2004, vol. 35 (6),
468 pp. 1889–1898.
- 469 [5] R. A. Vandermeer, B. Rath: *Metallurgical Transactions A* 1989, vol. 20 (10), pp. 1933–1942.
- 470 [6] R. A. Vandermeer, P. Gordon: *Trans. Aime* 1959, vol. 215, pp. 577–588.
- 471 [7] T. Sabin, G. Winther, D. Juul Jensen: *Acta Materialia* 2003, vol. 51 (14), pp. 3999–4011.
- 472 [8] A. Ridha, W. Hutchinson: *Acta Metallurgica* 1982, vol. 30 (10), pp. 1929–1939.
- 473 [9] F. Lin, Y. Zhang, N. Tao, W. Pantleon, D. Juul Jensen: *Acta Materialia* 2014, vol. 72, pp. 252–261.
- 474 [10] F. Humphreys: *Acta Metallurgica* 1977, vol. 25 (11), pp. 1323–1344.
- 475 [11] Y. Zhang, D. Juul Jensen, Y. Zhang, F. Lin, Z. Zhang, Q. Liu: *Scripta Materialia* 2012, vol. 67 (4), pp.
476 320–323.
- 477 [12] A. English, W. Backofen: *Trans. TMS-AIME* 1964, vol. 220, pp. 396–407.
- 478 [13] D. Juul Jensen: *Acta Metallurgica et Materialia* 1995, vol. 43 (11), pp. 4117–4129.
- 479 [14] K. Mukunthan, E. Hawbolt: *Metallurgical and Materials Transactions A* 1996, vol. 27 (11), pp. 3410–
480 3423.
- 481 [15] R. A. Vandermeer, R. Masumura, B. Rath: *Acta Metallurgica et Materialia* 1991, vol. 39 (3), pp.
482 383–389.
- 483 [16] E. Lauridsen, S. Schmidt, S. F. Nielsen, L. Margulies, H. Poulsen, D. Juul Jensen: *Scripta Materialia*
484 2006, vol. 55 (1), pp. 51–56.
- 485 [17] G. Wu, D. Juul Jensen: *Philosophical Magazine* 2012, vol. 92 (25-27), pp. 3381–3391.
- 486 [18] F. Lin, Y. Zhang, W. Pantleon, D. Juul Jensen: *Philosophical Magazine* 2015, vol. 95 (22), pp. 2427–
487 2449.
- 488 [19] C. M. Hefferan, J. Lind, S. F. Li, U. Lienert, A. D. Rollett, R. M. Suter: *Acta Materialia* 2012, vol.
489 60 (10), pp. 4311–4318.
- 490

- 491 [20] C. Xu, Y. Zhang, A. Godfrey, G. Wu, W. Liu, J. Z. Tischler, Q. Liu, D. Juul Jensen: Scientific reports
492 2017, vol. 7, pp. 42508.
- 493 [21] D. Field, L. Bradford, M. Nowell, T. Lillo: Acta Materialia 2007, vol. 55 (12), pp. 4233–4241.
- 494 [22] A. Vorhauer, S. Scheriau, R. Pippan: Metallurgical and Materials Transactions A 2008, vol. 39 (4),
495 pp. 908–918.
- 496 [23] F. Brisset, A.-L. Helbert, T. Baudin: Microscopy and Microanalysis 2013, vol. 19 (04), pp. 969–977.
- 497 [24] Y. Jin, B. Lin, M. Bernacki, G. S. Rohrer, A. Rollett, N. Bozzolo: Materials Science and Engineering:
498 A 2014, vol. 597, pp. 295–303.
- 499 [25] W. Truszkowski, J. Król, B. Major: Metallurgical Transactions A 1980, vol. 11 (5), pp. 749–758.
- 500 [26] F. Lin, T. Leffers, W. Pantleon, D. Juul Jensen: Effects of widening during rolling on the subsequent
501 recrystallization kinetics of copper: in: Materials Science Forum: Vol. 753: Trans Tech Publ, 2013:
502 pp. 285–288.
- 503 [27] G. Wu, D. Juul Jensen: Materials Characterization 2008, vol. 59 (6), pp. 794–800.
- 504 [28] E. E. Underwood: Stereology and Quantitative Metallography: ASTM International, 1972.
- 505 [29] S. O. Poulsen, E. M. Lauridsen, A. Lyckegaard, J. Oddershede, C. Gundlach, C. Curfs,
506 D. Juul Jensen: Scripta Materialia 2011, vol. 64 (11), pp. 1003–1006.
- 507 [30] Y. Zhang, A. Elbrønd, F. Lin: Materials Characterization 2014, vol. 96, pp. 158–165.
- 508 [31] A. Godfrey, W. Cao, Q. Liu, N. Hansen: Metallurgical and Materials Transactions A 2005, vol. 36 (9),
509 pp. 2371–2378.
- 510 [32] E. A. Jägle, E. J. Mittemeijer: Metallurgical and Materials Transactions A 2012, vol. 43 (4), pp. 1117–
511 1131.
- 512 [33] Y. Lü, D. A. Molodov, G. Gottstein: Acta Materialia 2011, vol. 59 (8), pp. 3229–3243.
- 513 [34] H. Chao, H. Sun, W. Chen, E. Wang: Materials Characterization 2011, vol. 62 (3), pp. 312–320.
- 514 [35] G. Speich, R. Fisher: Am. Soc. Metals, Metals Park, Ohio 1966, , pp. 563.
- 515 [36] R. A. Vandermeer, D. Juul Jensen: Acta Materialia 2003, vol. 51 (10), pp. 3005–3018.
- 516 [37] E. Villa, P. R. Rios: Acta Materialia 2009, vol. 57 (13), pp. 3714–3724.
- 517 [38] S. Storm, D. Juul Jensen: Scripta Materialia 2009, vol. 60 (7), pp. 477–480.
- 518 [39] R. Vandermeer: Acta Materialia 2005, vol. 53 (5), pp. 1449–1457.

- 519 [40] P. R. Rios, L. Pereira, F. Oliveira, W. Assis, J. Castro: *Acta Materialia* 2007, vol. 55 (13), pp. 4339–4348.
- 520 [41] P. R. Rios, R. Godiksen, S. Schmidt, D. Juul Jensen, R. Vandermeer: *Scripta Materialia* 2006, vol.
521 54 (8), pp. 1509–1513.
- 522 [42] B. Patterson, S. Grandhi: Stereological analysis of the effect of degree of cold work on nucleation
523 and growth rates during recrystallisation: in: *Proceedings of the 36th Riso International Symposi-*
524 *um on Materials Science: Roskilde, Denmark, 2015: p. 429–437.*
- 525 [43] A. Gokhale: *Metallurgical Transactions A* 1989, vol. 20 (3), pp. 349–355.
- 526 [44] Y. Zhang, A. Godfrey, Q. Liu, W. Liu, D. Juul Jensen: *Acta Materialia* 2009, vol. 57 (9), pp. 2631–2639.
- 527 [45] M. Cook, T. Richards: *J INST MET* 1947, vol. 73, pp. 1–31.
- 528 [46] D. Juul Jensen, T. Leffers: *Texture, Stress, and Microstructure* 1989, vol. 10 (4), pp. 361–373.
- 529 [47] F. Haessner, S. Hofmann: In: *Recrystallization of metallic materials.*(A79-22801 08-26) Stuttgart, Dr.
530 Riederer Verlag GmbH, 1978, p. 63-95. 1978, , pp. 63–95.
- 531 [48] A. Rollett, D. J. Srolovitz, R. Doherty, M. Anderson: *Acta Metallurgica* 1989, vol. 37 (2), pp. 627–639.
- 532 [49] M. Oyarzábal, A. Martínez-de Guereñu, I. Gutiérrez: *Materials Science and Engineering: A* 2008,
533 vol. 485 (1), pp. 200–209.
- 534 [50] B. Scholtes, R. Boulais-Sinou, A. Settefrati, D. P. Muñoz, I. Poitroult, A. Montouchet, N. Bozzolo,
535 M. Bernacki: *Computational Materials Science* 2016, vol. 122, pp. 57–71.
- 536 [51] L. Madej, M. Sitko, K. Radwanski, R. Kuziak: *Materials Chemistry and Physics* 2016, vol. 179, pp.
537 282–294.
- 538 [52] R. Doherty, I. Samajdar, C. Necker, H. Vatne, E. Nes: Nucleation of recrystallisation in cold and
539 hot deformed polycrystals: in: *Proceedings of the 36th Riso International Symposium on Materials*
540 *Science: Roskilde, Denmark, 1995: p. 1–23.*
- 541 [53] D. L. Olmsted, E. A. Holm, S. M. Foiles: *Acta Materialia* 2009, vol. 57 (13), pp. 3704–3713.
- 542 [54] P. A. Beck, P. R. Sperry, H. Hu: *Journal of Applied Physics* 1950, vol. 21 (5), pp. 420–425.
- 543 [55] G. Fan, Y. Zhang, J. H. Driver, D. Juul Jensen: *Scripta Materialia* 2014, vol. 72, pp. 9–12.
- 544 [56] Y. Zhang, J. Budai, J. Z. Tischler, W. Liu, R. Xu, E. Homer, A. Godfrey, D. Juul Jensen: *Scientific*
545 *reports* 2017, vol. 7 (1), pp. 4423.
- 546 [57] A. Gokhale, C. Iswaran, R. DeHoff: *Metallurgical Transactions A* 1979, vol. 10 (9), pp. 1239–1245.

547 [58] J. Christian: The Theory of Transformation in Metals and Alloys, Part 1: Pergamon, Oxford, 1981.

548 [59] Y. Zhang, A. Godfrey, D. Juul Jensen: Scripta Materialia 2011, vol. 64 (4), pp. 331–334.

549 Figure caption

550 Fig.1: Sketches showing the thermal treatments on the 90% cold-rolled plate. (a) Annealing for hardness
551 tests; (b) Annealing for post-mortem EBSD characterizations; (c) Annealing for in-situ 3DXRD measure-
552 ments; (d) Annealing for ex-situ EBSD characterizations.

553 Fig.2: (a) Vickers microhardness as a function of time for annealing at three temperatures. The error
554 bars show the standard error of the mean for measurements on the same sample. (b) Temperature
555 dependence of t_R , where t_R is the time for 50% hardness reduction.

556 Fig.3: Evolution of the recrystallized volume fraction (V_V), the interfacial area between recrystallized
557 grains and the deformed matrix per unit volume (S_V), and the contiguity ratio C_{RexRex} . (a) Avrami plot
558 showing $-\ln(1 - V_V)$ as a function of annealing time in a double logarithmic plot. (b) S_V as a function
559 of V_V . (c) VMR path plot: $S_V/(1 - V_V)$ vs. $-\ln(1 - V_V)$ in a double logarithmic plot. A solid line is
560 fitted in (c), from which the values of q and C in Eq. 8 are determined. In turn, these q and C values are
561 used to calculate the curve shown in (b). (d) Contiguity ratio C_{RexRex} vs. V_V . The solid line in (d) shows
562 the analytical prediction for random nucleation, and the dashed line represents $C_{\text{RexRex}} = V_V$.

563 Fig.4: Nucleation and growth results. (a) Number of recrystallized grains per unit volume N_V as a func-
564 tion of annealing time. Annealing twin boundaries (TB) are either ignored or included as normal grain
565 boundaries (GB) when determining the intercept length of the recrystallized grains D , which are used
566 in Eq. 4 to determine N_V . When twin boundaries are ignored, a grain and all of its twins are counted
567 as one grain, otherwise twins are counted as separated grains. (b) Cahn-Hagel boundary migration
568 velocity (G_{C-H}) as a function of annealing time. The fitted solid line in (b) has a slope of -0.92 ± 0.02 .

569 Fig.5: Increase of the equivalent sphere diameter (ESD) of individual grains as a function of annealing
570 time, measured by 3DXRD during in-situ annealing at 403 K. The arrow marks the growth curve of a
571 grain that continues to grow again after a stagnation period.

572 Fig.6: Growth of individual grains during ex-situ annealing at 423 K. (a)-(c) Orientation maps in the
573 deformed state (a) and after 10 min (b) and 35 min (c) annealing. Boundaries with misorientations larger
574 than 5° are shown in black. Twin boundaries are shown in white. (d) Boundaries with misorientation
575 larger than 5° within the deformed microstructure before annealing. Localized shear bands are marked

576 by arrows. (e) Contours of two recrystallized grains (A1 and A4) after 10 min and 35 min are shown on
577 top of the boundary map of the deformed microstructure.

578 Fig.7: Sketch showing the recrystallizing boundary positions for grains A1 and A4.

579 Fig.8: Stored energy density map. The local store energy density is represented in gray scale. The
580 recrystallizing boundaries of grains A1 and A4 after the first and the second annealing steps, and the
581 stationary boundaries are also shown. Two low E_s regions ahead of the stationary boundaries or invaded
582 by the recrystallized grains are indicated by arrows.

583 Fig.9: Distributions of misorientations between the recrystallized grains A1 (a) and A4 (b) and the in-
584 vaded deformed regions during the two annealing steps, and distributions of misorientations across
585 stationary recrystallizing boundaries for grains A1 (c) and A4 (d).

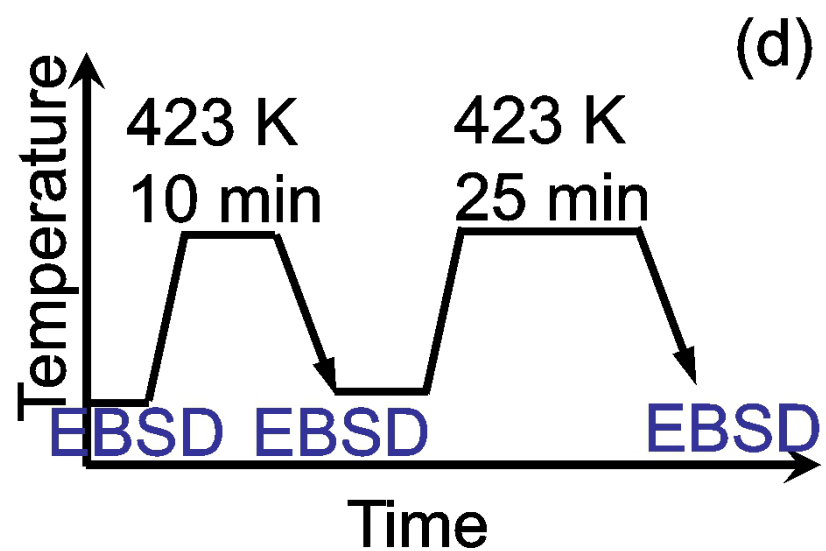
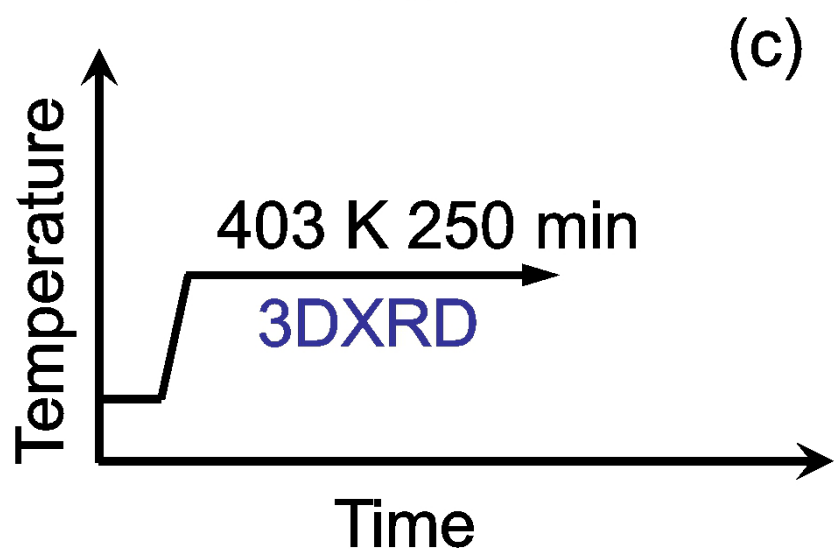
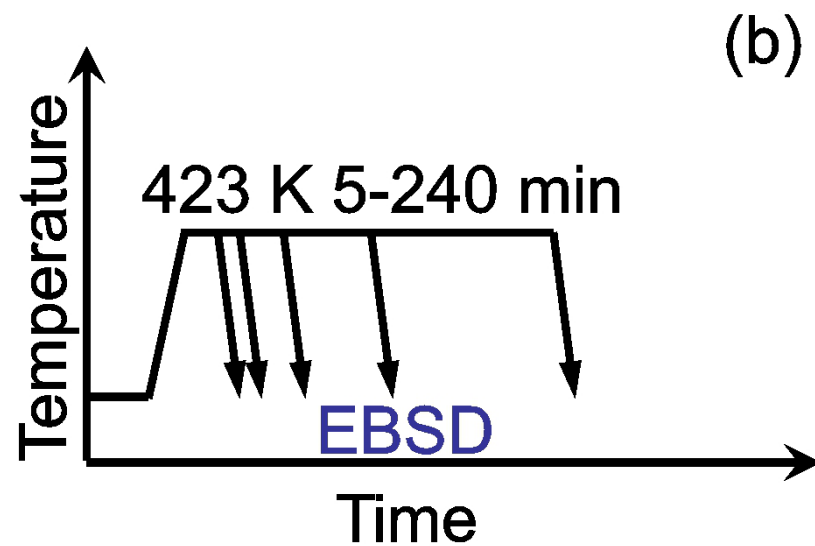
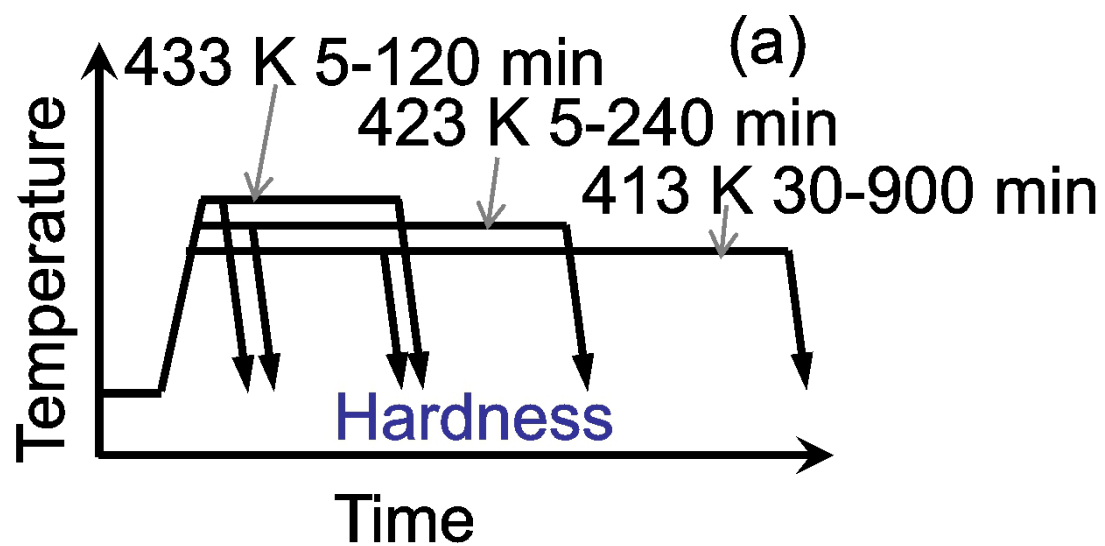
586 Fig.10: Sketch showing (a) low-dimensional, non-3D growth, (b) 3D growth with many stationary
587 boundary segments, and (c) 3D growth with boundary segments migrating at different velocities.

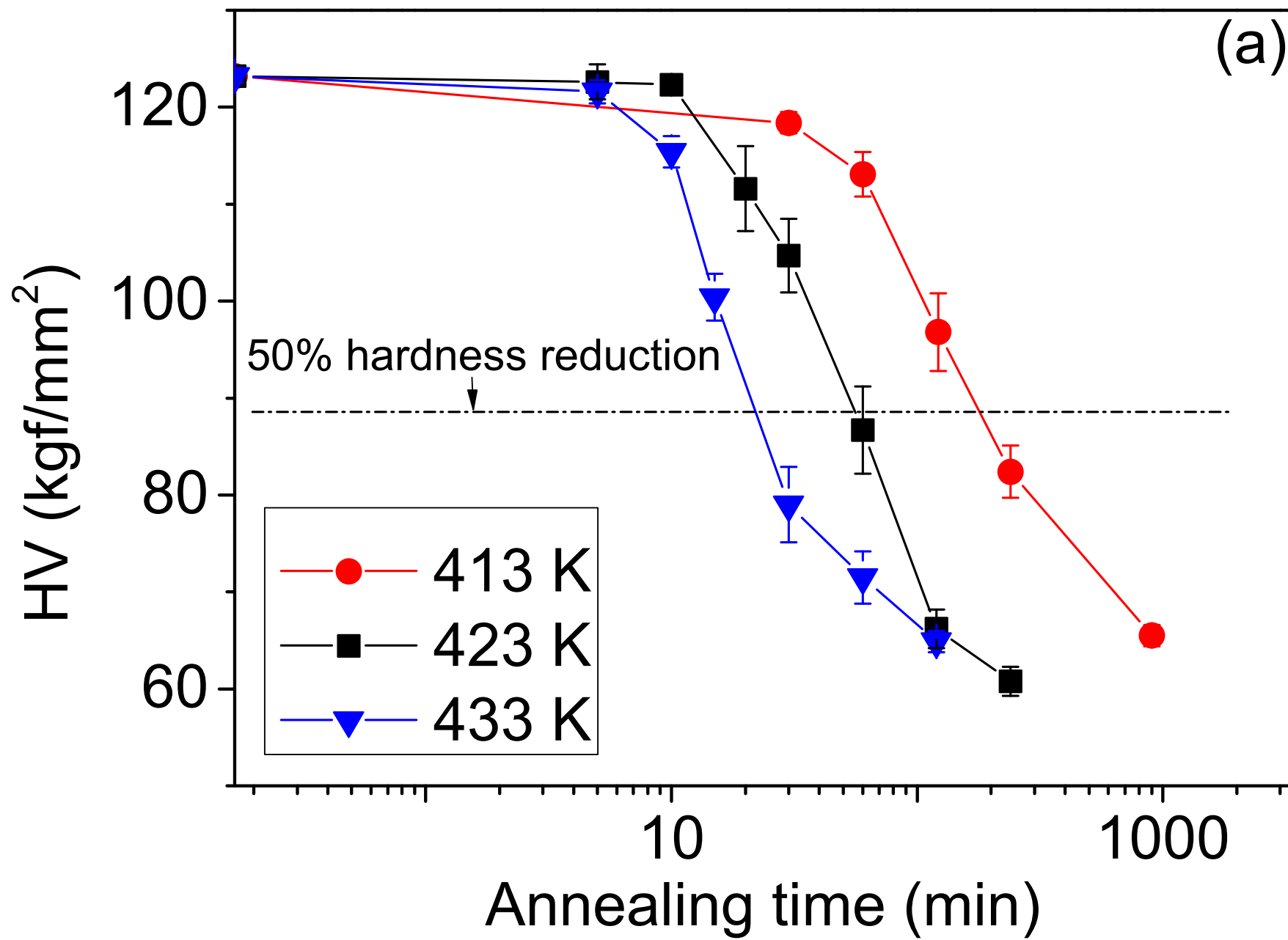
Table I: Chemical composition (weight percentage) of the material.

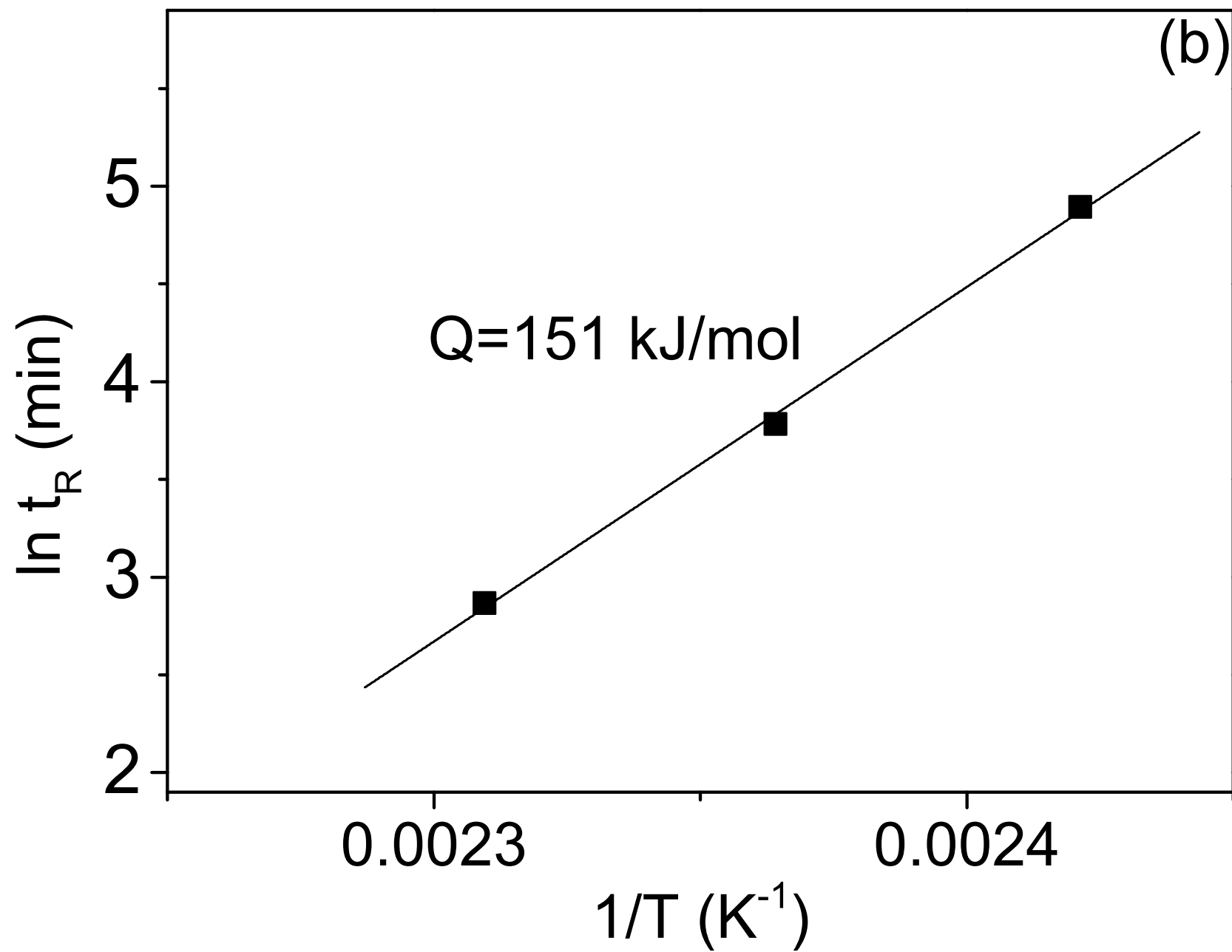
Cu	Ni(%)	Mg(%)	Al(%)
Balance	0.002	0.002	0.002

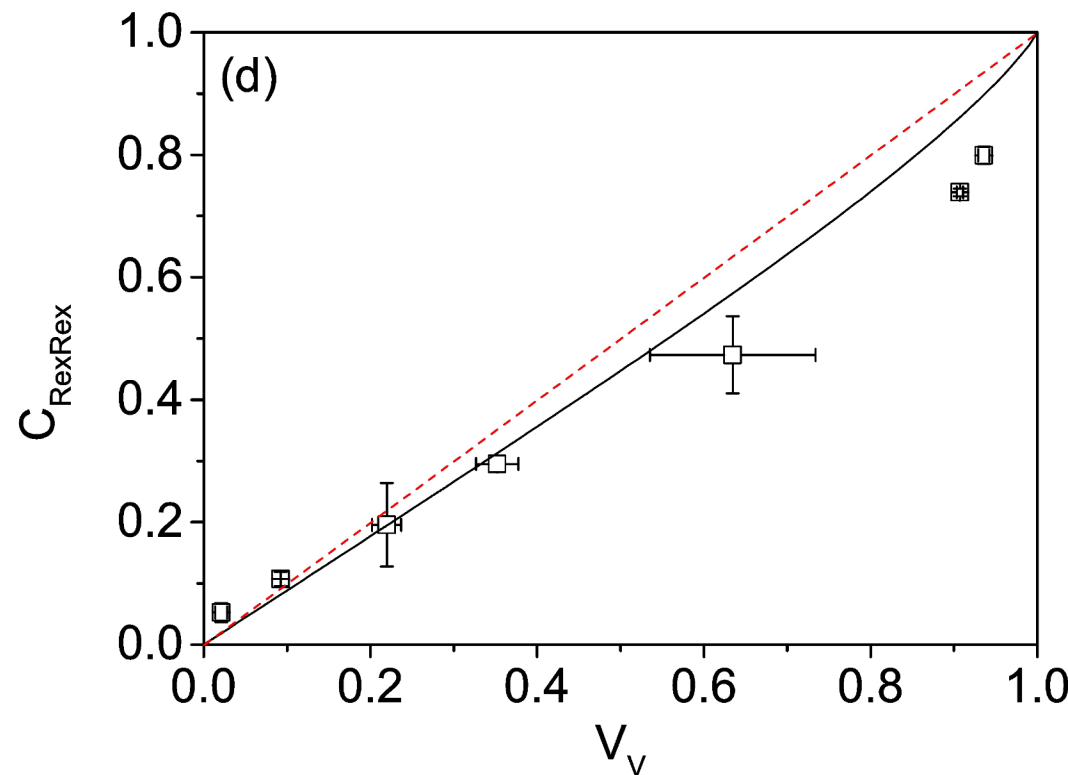
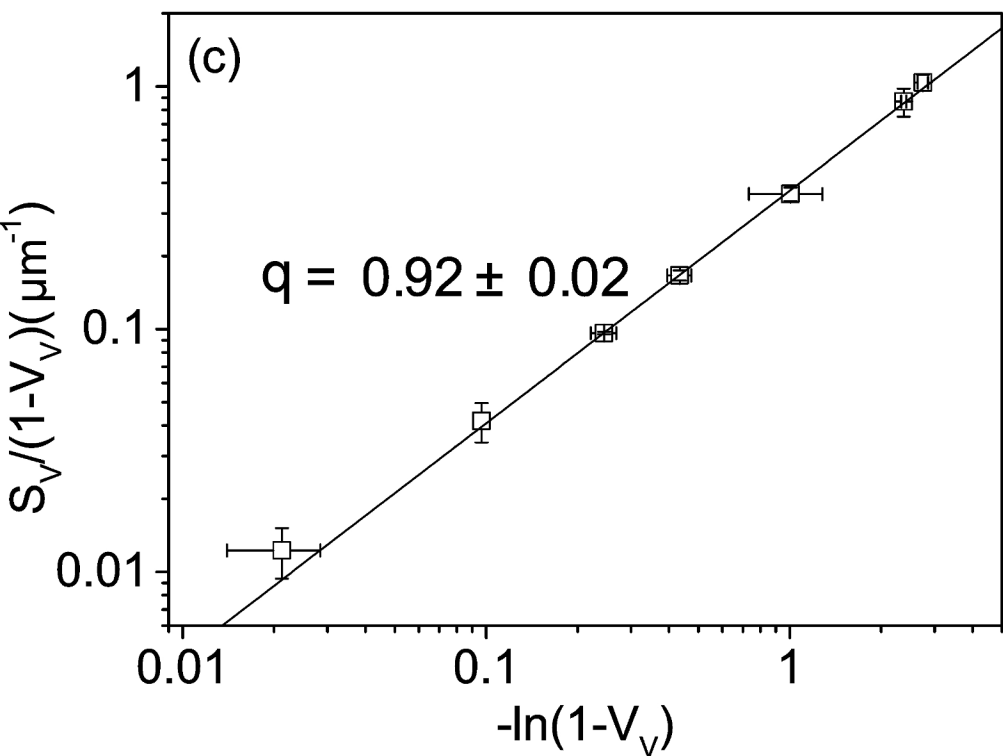
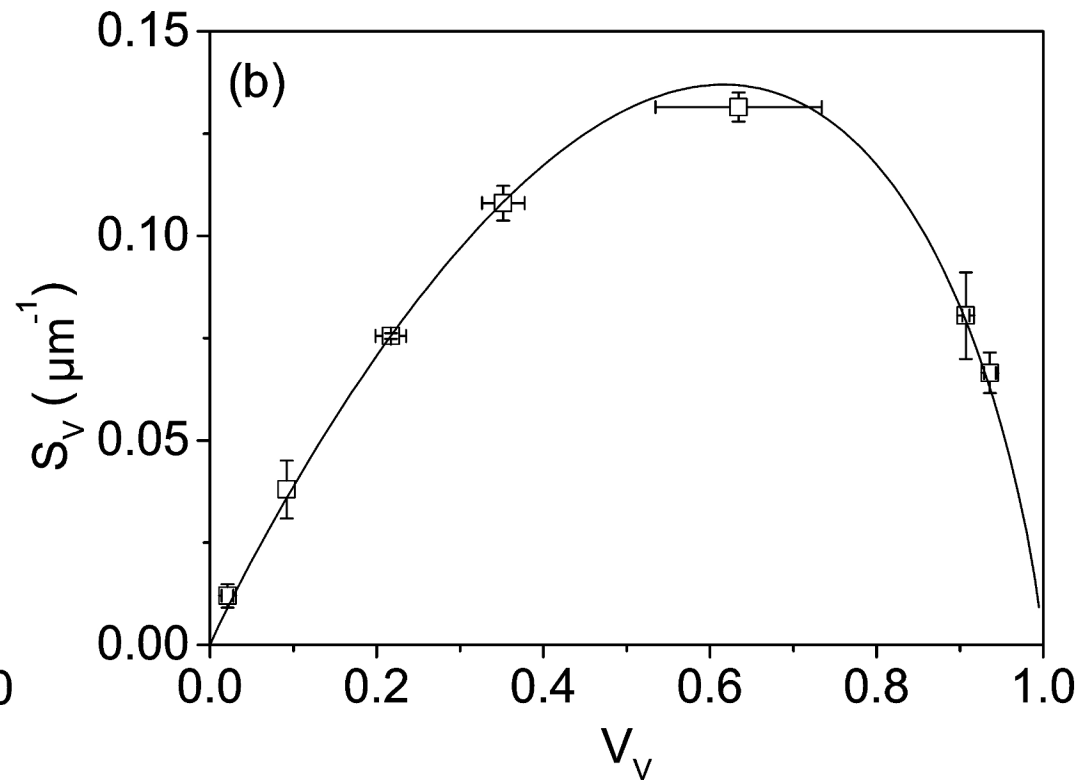
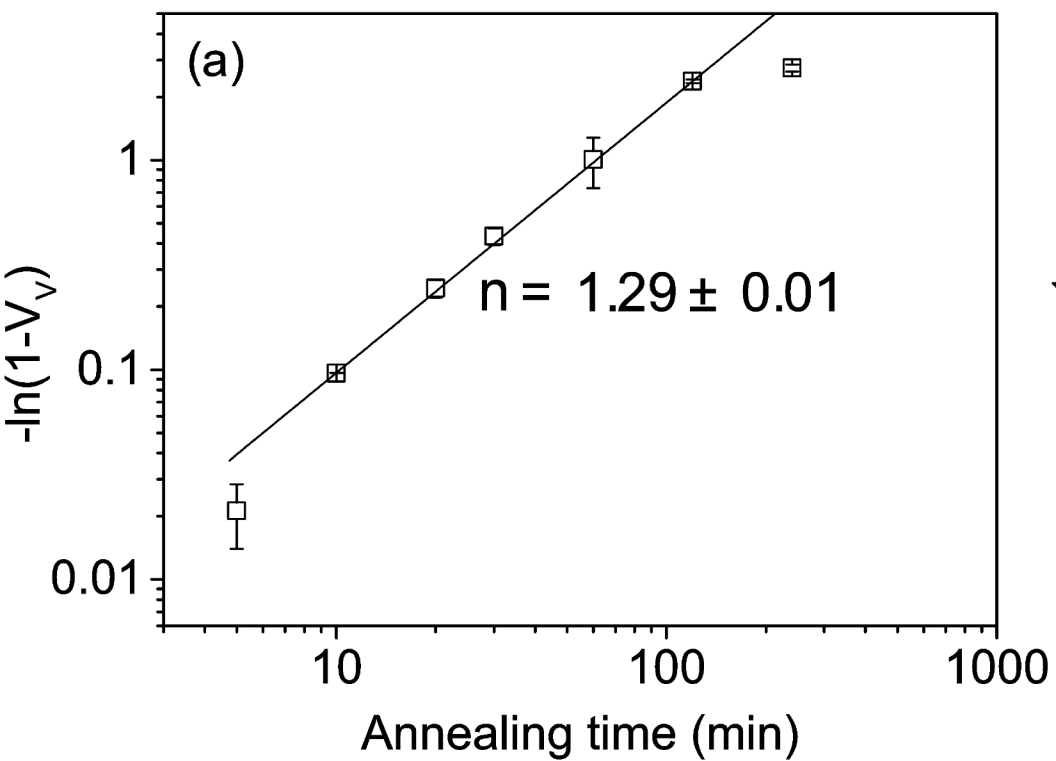
Table II: Grain areas and average stored energy density. $E_{s,mig}$ is the average stored energy density within the area that the migrating boundaries sweep during each annealing step. $E_{s,sta}$ is the average stored energy density in the area ahead of the stationary boundaries.

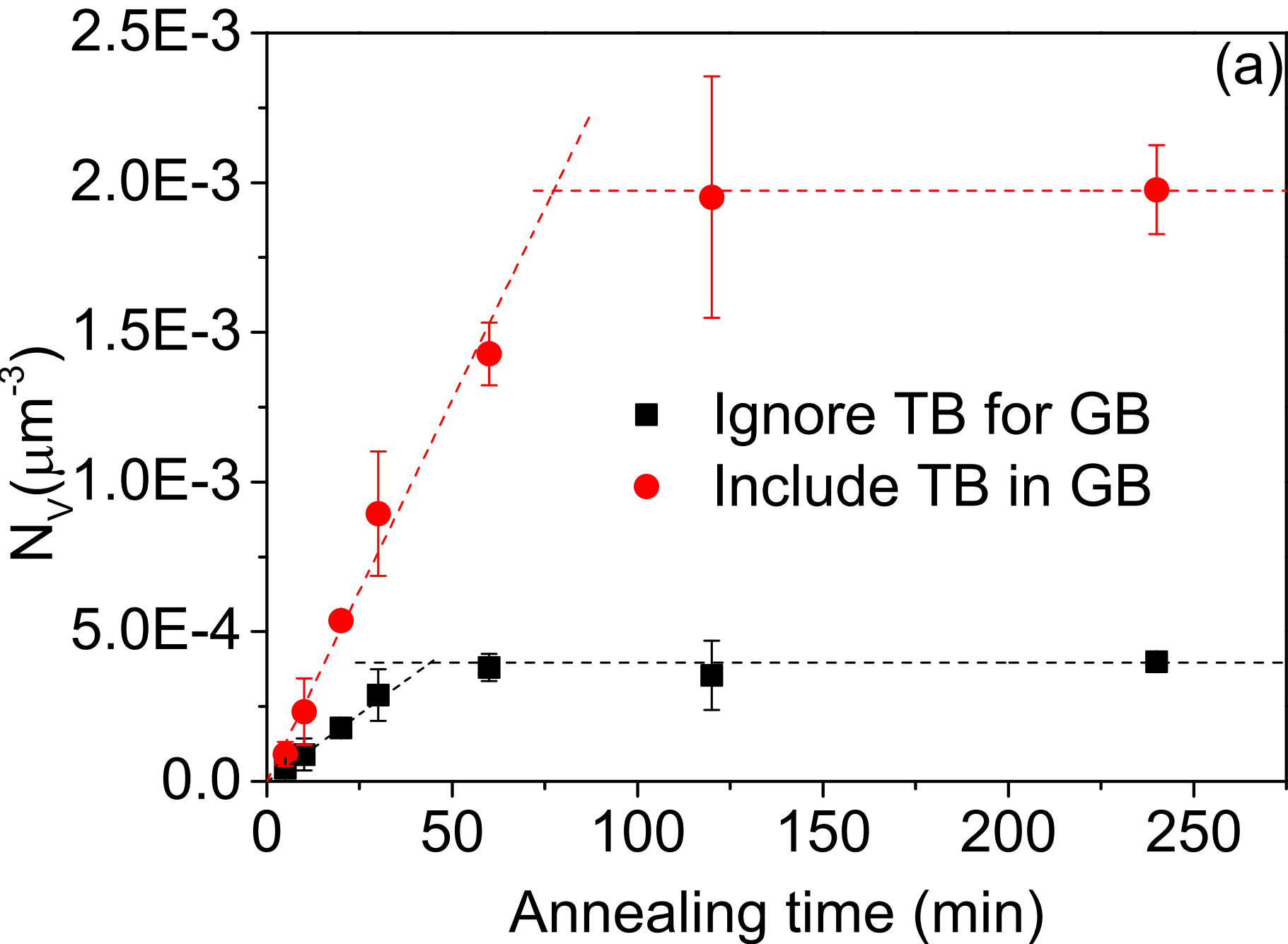
	Grain A1			Grain A4		
	Area (μm^2)	$E_{s,mig}$ (MJ/m ³)	$E_{s,sta}$ (MJ/m ³)	Area (μm^2)	$E_{s,mig}$ (MJ/m ³)	$E_{s,sta}$ (MJ/m ³)
Step 1 (0-10 min)	81.5	3.3		7.0	2.7	
Step 2 (10-35 min)	392.2	3.1	2.7	25.3	2.9	3.1

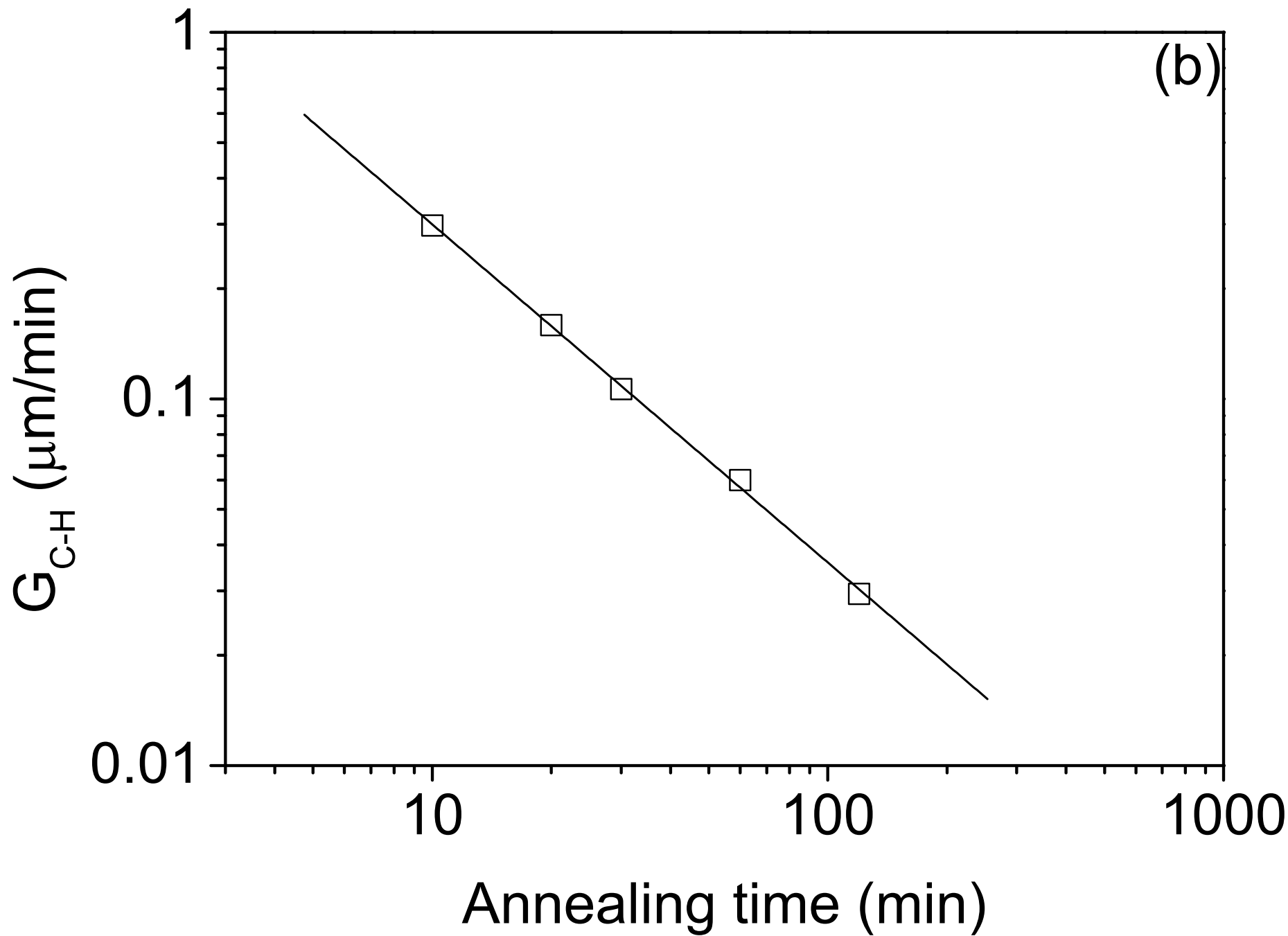


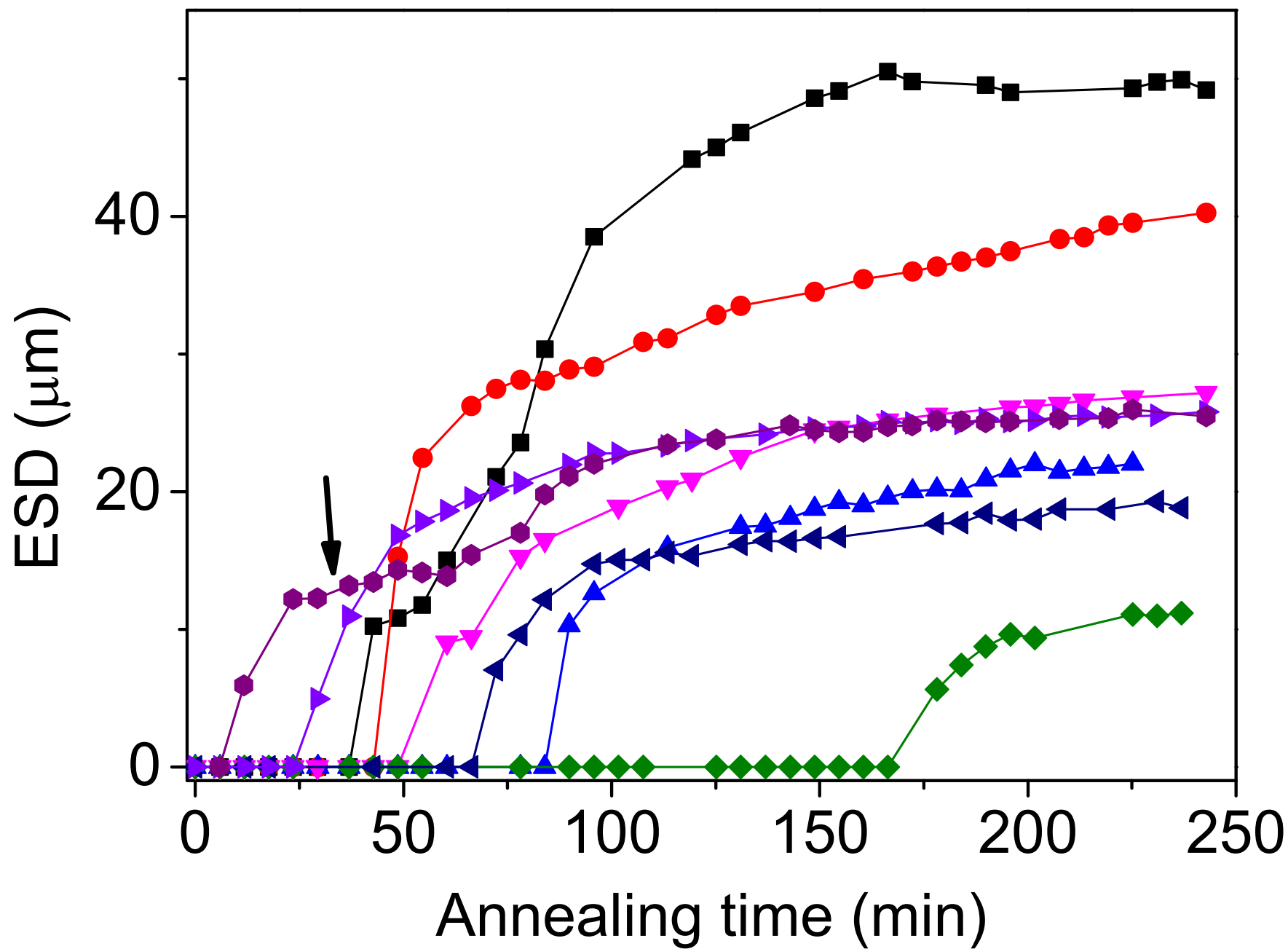


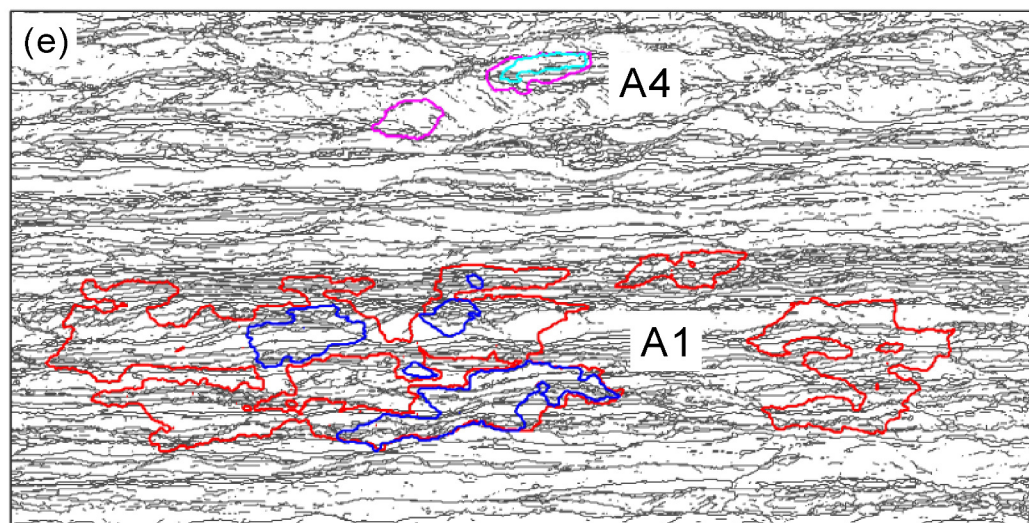
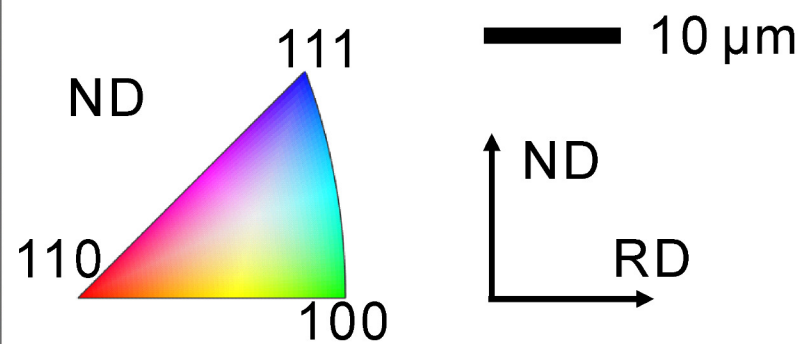
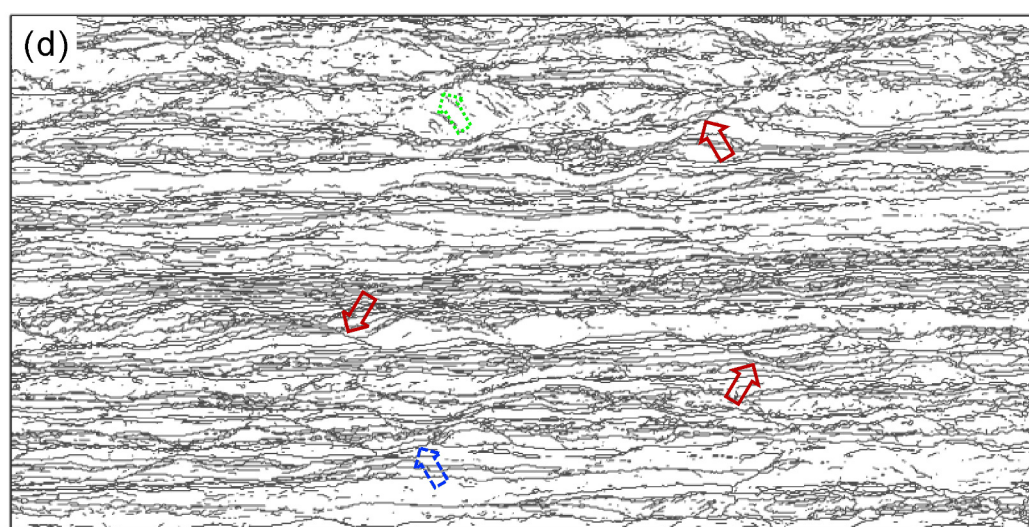
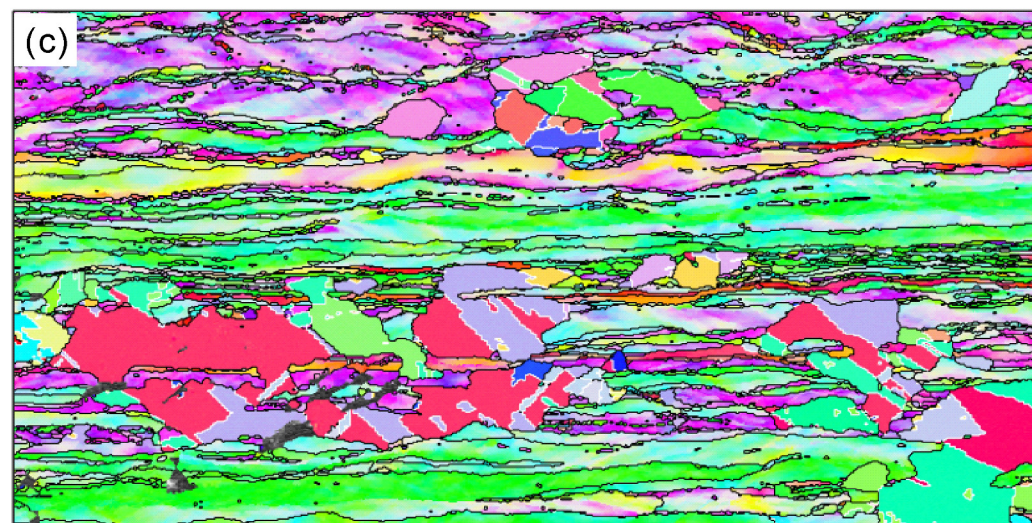
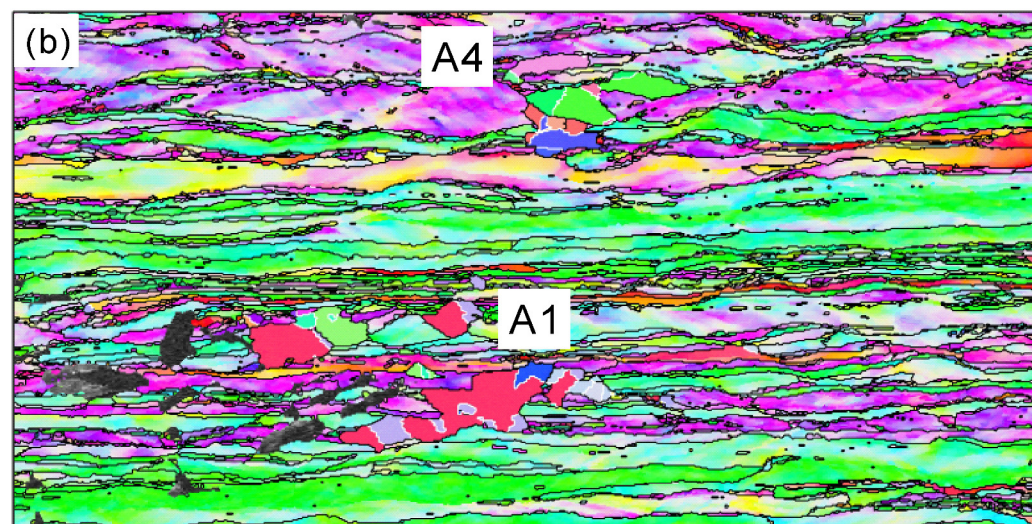
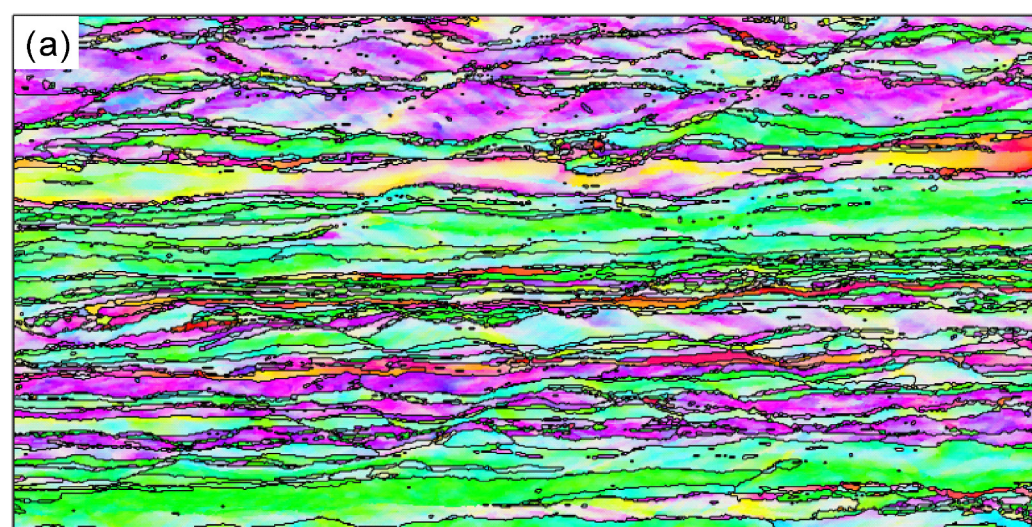














10 μm

